MAESTRÍA EN PROCESAMIENTO DE SEÑALES E IMÁGENES DIGITALES

ESCUELA DE POSGRADO
PONTIFICIA UNIVERSIDAD CATÓLICA DEL PERÚ

Evaluation of Elastographic techniques generated by means of external vibration

Submitted by
Johnny Junior Arroyo Barboza

In partial fulfillment of the requirements for the Degree of
Master in Digital Signal and Image Processing
in the Graduate School of the Pontificia Universidad Católica del Perú.

Thesis supervised by:
Benjamin Castañeda Aphan, Ph.D.
Tim Salcudean, Ph.D.

Examining commitee members:
Benjamin Castañeda Aphan, Ph.D.
Tim Salcudean, Ph.D.
Clark Wu, Ph.D.

Lima, Perú
September 6, 2017

Abstract

Breast cancer is one of the greatest problems of national and international public health, whose incidence among women population shows an increasing trend. Nowadays there are several elastographic techniques, which seek to characterize the tissue, that is, to analyze the response produced by the application of a perturbation in the medium, to describe its mechanical properties. Among the modalities used are ultrasound, nuclear magnetic resonance and optical coherence tomography. On the other hand, among the types of disturbance used are low frequency mechanical waves, a uniform compression force or acoustic radiation force.

In this thesis work, ultrasound was used due to its low economical cost in comparison to the other modalities. In addition, the type of perturbation selected was the external mechanical vibration, as it ensures the achievement of quantitative results, there is no risk of temperature rise in the analyzed area and allows the repeatability of the results obtained. Hence, two elastographic techniques were the axes of the present work: vibro-elastography and normal vibration holography. For the first, a calibrated phantom and a gelatin-based phantom were used, in order to characterize and validate the technique over a wide range of excitation frequencies. Posteriorly, 18 patients were analyzed prior biopsy exam, obtaining elastograms and contrasting them with the respective biopsy results. The results suggest that the technique is able to identify the presence of benign or malignant cancer, and the elasticity estimated agree with values reported in the literature. The second technique is proposed in the elastography field for the first time. Based on holography, its experimental scheme is established, and the mathematical expression for shear speed estimation is presented. Results from simulation and experiments performed on homogeneous and heterogeneous phantoms are presented, and the estimates are compared with previously obtained reference values. The results suggest that the estimates are close to the reference values for all media tested, and the technique must be studied in depth to revert artifacts formation.

For being there when I arrived at midnight or left at dawn, for all the effort made for me during 24 years, and for always giving me the calmness I needed. This work is dedicated to my mother Nelsa, my father Vicente and my sister Andrea.

Also, a person who has been my motivation during the development of this work, who kindly helped me in all aspects, motivated me when my spirit waned, for the happy moments that we have lived and will live. To you, Ana Cecilia. I owe you much of this.

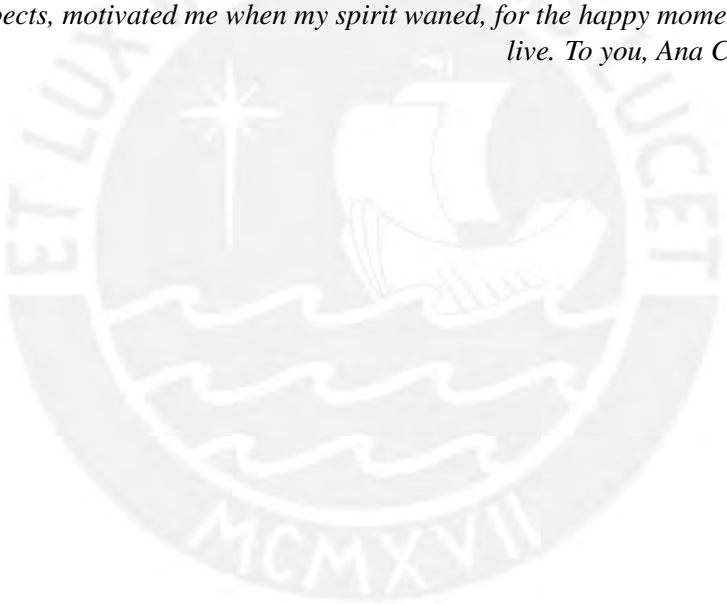

Acknowledgments

This work closes a stage that some time ago I did not think to live, but that fortunately happened. Of course, it would have been impossible to do this work for myself. I want to thank my family, who were a great support in all senses for me. To Ana Cecilia, who has been my ideal right hand person throughout this stage. To professors Benjamin Castañeda and Roberto Lavarello, for encouraging me and giving me the opportunity to enroll in the master program, for help me to get the opportunity to be present at an international conference, for the constructive criticisms that were certainly very useful, as well as for the confidence offered . To M.Sc. Julio Lobo and professor Tim Salcudean from the Universitiy of British Columbia, for the feedback provided and for always being willing to collaborate with me. To the members of the laboratory, in which I found good friends, inside and outside the academic field. I'm sure the friendship will last. To the Laboratorio de Materiales from the PUCP, for the aid in the realization of mechanical experiments included in the work. Finally, thanks to my funding sources: Fondo Nacional de Desarrollo Cientifico y Tecnologico-PERU under Grant 012-2014-FONDECYT-C1 from the Peruvian Government.

Contents

List of Figures

List of Tables

Chapter 1

Introduction

Breast cancer is a public health problem worldwide, whose prevalence on the population is growing. According to the American Cancer Society, breast cancer in United States leads the statistics corresponding to the estimated new cases and deaths among women population, reaching 30% and 25% respectively [1]. In Peru, it shows the second highest incidence (16.6%) behind cervical cancer [2]. Generally, this disease manifests itself through internal and external physical changes of the breast. Symptoms that require further analysis are bloody secretions, localized temperature change, pain, skin texture change and the appearance of stiff masses in the breast.

Given that the change in the pathological state of soft tissue is related to the presence of a disease [3] (such as tumor appearance or growth), palpation has been commonly used by clinicians for cancer diagnosis. In spite of its invaluable contribution over the years, it requires specific conditions to be able to perform the detection of cysts or abnormal masses. For example, the lesion should be located close to the surface of the tissue, exhibit a considerable elasticity contrast with respect to the surrounding healthy tissue and not be so small [4]. Biopsy is an invasive and operator-dependent procedure currently considered as the gold standard for diagnosis. Nevertheless, it also presents many disadvantages. First of all, its invasiveness. To perform the intervention, a small section of tissue is extracted by using a thin needle. Since not all tumors located in the breast can be seen clearly by ultrasound, it can lead to a sampling error at the time of the biopsy. Since not all tumors located in the breast can be clearly seen by ultrasound, it can lead to a sampling error during the biopsy. This means that there is some risk of removing healthy tissue rather than cyst tissue, yielding misleading results. In addition, side effects such as bleeding and pain may occur near the puncture site. Likewise, the results are qualitative, not quantitative. Finally, there is a cost associated with conducting the exam.

For all of the above, it was necessary to develop a technique that has the same virtues of biopsy, but whose application is non-invasive. Based on the fact that the pathological state of a tissue is related to its mechanical properties (viscosity, elastic modulus, among others), as well as the availability of medical imaging modalities that allow visualizing the internal structure of the organism, the elastography began to developing rapidly. Several investigation groups have directed their efforts in developing elastography methods for tissue characterization, based on different imaging modalities such as ultrasound [5, 6], magnetic resonance imaging [7] and optical coherence tomography [8]. They were tested and applied for cancer detection and diagnosis (liver, prostate, breast, thyroid), hepatic fibrosis and steatosis - which are indicative in turn of cirrhosis and hepatitis -, musculotendinous and neuromuscular disease, arterial wall stiffness and plaque evaluation, among others. Despite the variety, they all share the same principle: creating a disturbance in the tissue, observing and processing the originated

response. From this, to infer the mechanical properties of the tissue, to finally show the results by means of an image.

A fundamental classification between the elastography techniques can be done based on the type of excitation used to generate the perturbation: quasi-static methods, that apply uniaxial compression; transient methods, which use pulses of short duration to generate shear waves and analyze the tissue, and finally steady-state methods, which induce external harmonic excitation, producing a pattern of temporal displacement on the medium.

Modern commercial scanners have elastography implementation for real-time visualization, particularly for quasi-static methods (Strain Imaging) and transient methods (Acoustic Radiation Force Imaging) [9, 10]. On the one hand, the disadvantage presented by quasi-static implementations is the inability to provide quantitative results. Once the compression is exerted on the tissue, the strain is calculated based on the reference and compressed image, which reveals relative stiffness of the analyzed region. In the other hand, the disadvantage of ARFI lies in the time required to image the entire region. The imaging process consist on emitting pushing beams of focused ultrasound waves, which must vary its lateral position in order to cover a 2D region. The thermal increase in the tissue for a single pushing beam can be negligible, nevertheless the cumulative effect when acquiring a 2D image in real time can cause a bigger impact in heating [11, 12].

Most of steady-state techniques implemented in ultrasound scanners have been applied to the diagnosis of liver cancer [13, 14] and breast cancer [15, 16, 17], which mostly employ acoustic radiation force, but not external vibration. In this thesis, the evaluation of techniques that can produce quantitative results without inducing heat in the tissue is of major interest. These must meet the requirement of being a steady-state method and make use of external vibrators to induce mechanical excitation in the tissue.

1.1 Objectives of the thesis

This thesis focuses on the evaluation of two elastography techniques based on external vibration application: Vibro-elastography and Normal Vibration Holography.
First, to integrate the hardware and software of Vibro-elastography to the SonixTouch ultrasound system, in order to perform experiments with the technique. Second, after the integrated system was put into operation, to carry out phantom experiments to evaluate Vibro-elastography through lateral resolution, contrast to noise ratio, signal to noise ratio, contrast and accuracy. Third, to work with Vibro-elastography to carry out experiments on volunteer patients of the Health Care Oncosalud. Then, to obtain elastograms from the acquired data and to compare the obtained results with the results of the biopsies. Finally, to present and to implement Normal Vibration Holography, a technique based on the experimental scheme from Shear Wave Holography technique. Once it is implemented, to perform simulations and experiments on gelatin-based phantoms.

1.2 Organization: outline

The thesis is organized as follows: Chapter II reviews elastography and the procedure that several techniques use to infer viscoelastic properties of the tissue. Additionally, the theory of mechanical measurements to establish the reference value of phantoms and the metrics used to evaluate the elastograms are presented. In Chapter III Vibro-elastography is introduced , starting with the theory and then showing the experiments performed on a calibrated breast phantom and an ex-vivo pig kidney. In Chapter IV the experiments in patients are explained in detail, showing the elastograms obtained and a

classification diagram between benign and malignant cancer cases. Chapter V corresponds to Normal Vibration Holography, where simulations are described and the experiments carried out are presented. Finally, in Chapter VI the final ideas and conclusions are developed.

Chapter 2

Theory

2.1 Elastography

Elastography is a field of medical imaging, which aim is to differentiate the viscoelastic properties of the normal and diseased tissue, attempting to provide clinically relevant information.

2.1.1 General Overview

Roughly, its general principle consist on excite the tissue, producing a vibration in the internal structure. This is measured by using a sensor, to infer later the viscoelastic properties by adopting a mechanical model of the examined material.

In general, it allows to visualize the mechanical properties of soft tissue in a qualitative (relative stiffness) or in a quantitative (absolute stiffness) fashion. This depends on the excitation force and the further processing applied. From the general principle stated, a fundamental classification between the elastographic techniques can be done based on the type of excitation used.

2.1.2 Quasi-static techniques

Describes the induced strain in the underlying tissue produced by a purely uniaxial compression. Hence, a small displacement will occur in the axial direction, which can be estimated by cross-correlating small segments of pre and post-compressed RF signals [19]. The harder regions are expected to move less than the softer regions for the same compression force, which allows to differentiate abnormal masses in a region of interest.
From Hooke's law, the relation between stress(ε) and strain(σ) is given by

$$E = \frac{\sigma}{\varepsilon}, \tag{2.1}$$

Nevertheless, to perform the internal stress measurement is a difficult task. In that sense, a typical solution is to assume a uniform stress distribution, which can be achieved by using a compressor with a large footprint (commonly, the ultrasound probe is used for this purpose, exerting a quasi-static pressure field in the surface of the tissue). Since the magnitude of the distribution is unknown, only a relative estimation can be performed, yielding qualitative results.

One of the first examinations that were carried out using this technique was in breast, trying to determine the potential of its application in the detection of lesions [20]. This technique was seen as

freehand palpation, analyzing conditions that provided good elastograms, such as the position of the patient or the direction of compression [21]. Finally, characteristics such as viscoelasticity to characterize the breast have also been studied and reported [22].

2.1.3 Transient techniques

A simple way to calculate the tissue stiffness is by estimating the speed at which shear waves propagates through the medium. Transient techniques take advantage of this approach, and use a short-term excitation (impulse signal) to generate shear waves. Depending on the tissue stiffness, the produced shear waves will present a speed ranging from $1 - 10$ m/s, being necessary a high rate to monitor the movement properly. The impulse signal can be created by an external mechanical source, or by an acoustic radiation force (ARF), where several pushing beams are generated and transmitted sequentially, each one at a slight different lateral location than the previous one, to interrogate an entire 2D ROI. Currently there are commercial scanners that include this modality. Its application is mainly aimed at detecting liver fibrosis, obtaining better results than other modalities [23, 24]. However, it presents some limitations when applied clinically, such as being able to explore only a small portion of the mammary parenchyma, being susceptible to error in case of obesity, as well as the lack of support for some B-mode image while examining the tissue [25]. Moreover, it has been reported that it is not entirely accurate when examining cases of acute liver damage [26, 27].

During the last years, quantitative techniques have been developed with the same idea of the qualitative transient techniques: emission of pulses by means of acoustic radiation force. The difference lies in the monitoring technology and the processing applied. On the one hand, Shear Wave elastography Imaging (SWEI) [28] is based on the emission of laterally propagated shear waves from the initial pulse, which makes it possible to generate elasticity images. On the other hand, Supersonic Shear Imaging (SSI) uses a large number of simultaneous pulses close together, generating a source of shear waves that propagate through the tissue at supersonic speed. It is then monitored using the ultrafast imaging technique [29].

2.1.4 Steady-state techniques

These techniques apply a dynamic harmonic external excitation on the tissue, which ranges between 100 -1000 Hz, producing a sequence of displacement in time. After analyzing the displacement profile and completing the post-processing step, the shear wavelength or wave number is estimated, relating it to the elastic parameters using any speed estimator (Phase derivative, Local Frequency estimators, among others). Final results are quantitative. Within these techniques are Crawling waves [30], Shear wave holography [30] and Vibro-elastography [31].

It has been shown in [32] that quantitative measurements from steady-state techniques can reduce dependence on operator intervention and improve repeatability.

2.2 Mechanical Measurements

The elastographic techniques undergo an initial experimentation test on phantoms, either in calibrated or in gelatin-based ones. For calibrated phantoms, the manufacturer provides certified values of elasticity for both background and inclusions. On the other hand, in gelatin-based phantoms, the most common way to obtain values that serve as a reference is through mechanical measurement of stress-relaxation tests.

Understanding the mechanical behavior of soft tissue is of great interest. Nonetheless, it appears as a challenging task, since it presents mechanical and geometric non-linearities, a viscoelastic behavior and boundaries generally not well defined. Several viscoelastic constitutive classic models have been defined and widely studied, such as the Zener, Maxwell and Kelvin-Voigt. All of them uses a series of springs, masses and dashpot elements in different combinations, which basically pretend to simulate the tissue response when subjected to an external force. The advantage that they present is to allow forming simple models that are adjusted greatly to the experimental data. With the aim of better adjusting to the experimental results, it is recurrent to increase the parametric dimensions of the model, which makes it difficult to translate this into a mechanical model.
A solution is to use Fractional-Derivative models, which fit closer to the experimental data than integer-order models, and require a smaller number of parameters. Kumar *et al.* [33] showed that the Kelvin-Voigt Fractional Derivative model provides a better fit than the other models. The model is used to fit experimental results in this work.

2.2.1 The Kelvin-Voigt Fractional Derivative model

This model characterizes the time dependent-relaxation behavior of viscoelastic samples when subjected to an external force. It uses three parameters: E_0 (relaxed elastic constant), η (viscoelastic parameter) and α (order of the fractional derivative).

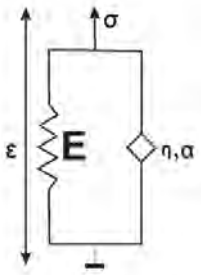

Figure 2.1: Representation of the Kelvin Voigt Fractional Derivative model. A fractional derivative term is included to reduce the number of the parameters required for a good fitting to the experimental data.

The model is shown in Figure 2.1, and relates the stress (σ) and strain (ε) according to

$$\sigma(t) = E_0\varepsilon(t) + \eta D^{\alpha}[\varepsilon(t)], \tag{2.2}$$

where t refers to the time and D^{α} to the fractional derivative of order α. This, in turn, is represented by

$$D^{\alpha}[x(t)] = \frac{1}{\Gamma(1-\alpha)} \int_0^t \frac{x'(\tau)}{(t-\tau)^{\alpha}} d\tau, \tag{2.3}$$

where Γ is the Gamma function, and α takes a value between $[0,1]$.

2.2.2 Stress Relaxation test

To start modeling the sample, and following the analysis performed by Zhang *et al*. [34], it is assumed that the strain distribution follows a ramp function of duration T_0, after which a constant strain ε_0 is maintained.

$$\varepsilon(t) = \begin{cases} (\frac{t}{T_0})\varepsilon_0 & \text{if } 0 \leq t \leq T_0 \\ \varepsilon_0 & \text{when } t \geq T_0 \end{cases} \tag{2.4}$$

Applying Laplace transform to Equation 2.2, 2.3 and 2.4, expressions for stress and strain can be obtained. After mixing them and returning to the temporal domain, Equation 2.5 is obtained

$$\sigma(t) = E_0\varepsilon(t) + \eta\frac{\varepsilon_0}{\Gamma(2-\alpha)T_0}(t^{1-\alpha} - (t-T_0)^{1-\alpha}), \tag{2.5}$$

2.2.3 Frequency response

The sample response for each frequency can be determined by converting Equation 2.2 to the frequency domain, through Fourier Transform.

$$\sigma(\omega) = E_0\varepsilon(\omega) + \eta(j\omega)^{\alpha}[\varepsilon(\omega)], \tag{2.6}$$

If the radial frequency is required to be positive, and considering $\omega = 2\pi f$, the complex modulus is

$$E^* = \frac{\sigma(f)}{\varepsilon(f)} = [E_0 + \eta cos\left(\frac{\pi\alpha}{2}\right)(2\pi f)^{\alpha}] + j[\eta sin\left(\frac{\pi\alpha}{2}\right)(2\pi f)^{\alpha}] \tag{2.7}$$

where the real part is the storage modulus, and the imaginary part is the loss modulus.

2.3 Time of Flight measurement

To validate the estimates made by an elastographic technique, the time of flight experiment (ToF) is also often used to find a reference speed value. The value obtained represents the speed at which a single pulse travels across the medium. Its scheme is shown in Fig. 2.2, where the phantom is placed between two shakers, one used as an emitter and the other one as a receiver. The emitted and received pulses were visualized in an oscilloscope, determining the time the pulse requires to reach the opposite end. By calculating the distance between the emitter and receiver plates (Δx) and the arriving time (Δt), the expected shear speed can be estimated according

$$c_s = \frac{\Delta x}{\Delta t}, \tag{2.8}$$

2.4 Evaluation metrics

With the purpose of evaluating the quality of the images as well as the elasticity estimation capacity of the technique, several metrics are proposed.

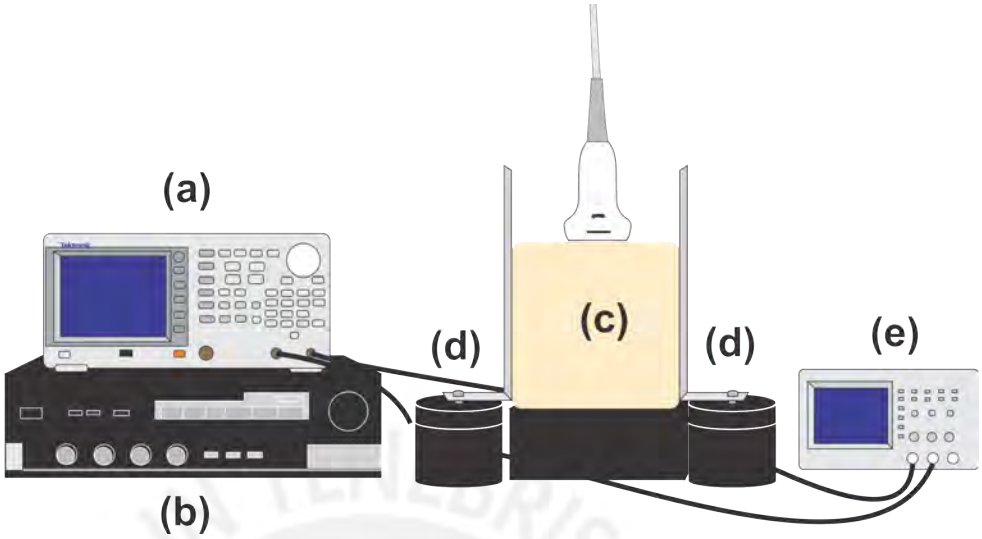

Figure 2.2: Experimental scheme used for time of flight measurement. A signal generator (**a**) was connected to an amplifier (**b**), to propagate a pulse across the phantom (**c**), which is placed between two vibrators (**d**). The emitted and received signals are analyzed using an oscilloscope (**e**).

2.4.1 Lateral resolution

The lateral resolution is the ability of an imaging system to correctly distinguish two horizontally located points rather than considering them as one. It is usually measured in units of space, and the higher the estimated value of lateral resolution, the less the ability to distinguish both points.

To measure the lateral resolution in an elasticity image, a profile passing through the center of the inclusion is selected and then fitted to a double sigmoid function, given by

$$c(x) = (c_{in} + c_{out}) \left(\frac{1}{1 + e^{\frac{x_1 - x}{\lambda_1}}} \right) \left(\frac{1}{1 + e^{\frac{x - x_2}{\lambda_2}}} \right) + c_{out}\,, \tag{2.9}$$

where c_{in} and c_{out} refers to the elasticity value inside and outside the inclusion respectively, x_1 and x_2 are the inclusion boundaries and λ_1 and λ_2 are the transition width from background-inclusion and vice versa.

From the model, it should be possible to extract the fitted values for λ_1 and λ_2. They define the resolution R_{2080}, which reflects quantitatively the distance required for a 20-80% transition in the elasticity values.

$$R_{2080,i} = 2\ln(4)\lambda_i, i = 1,2, \tag{2.10}$$

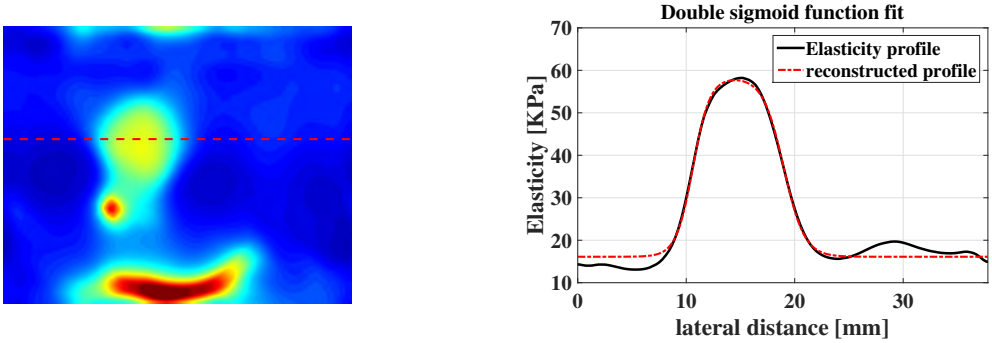

(a) (b)

Figure 2.3: (a) Elasticity image with a hard inclusion. The plotted horizontal line passes through the center of the inclusion. (b) Double sigmoid fitting from the profile selected in the elasticity map. From the fitting, the required parameters can be obtained.

2.4.2 Contrast, SNR, CNR and accuracy estimation

SNR:
The SNR is a measure that compares the signal level of the elastogram with the noise level present in the image. Its mathematical expression is given by

$$SNR = 20\log_{10}\left(\frac{\mu}{\sigma}\right) \tag{2.11}$$

where μ and σ make reference to the mean and standard deviation value respectively in the final elastographic image.

CNR:
The CNR is very similar to the SNR, with the difference that the measurement is based more in contrast than in the raw signal.

$$CNR = 20\log_{10}\left(\frac{2(\mu_1-\mu_2)^2}{\sigma_1^2+\sigma_2^2}\right), \tag{2.12}$$

where μ and σ make reference to the mean and standard deviation value respectively in the final elastographic image, subscript (1) for inclusion and (2) for background.

Contrast:
The contrast is a metric that is based on comparing the estimates of two regions within an image, and thus measure the level of distinction between both.

$$Contrast = \frac{|\mu_1-\mu_2|}{\mu_2}. \tag{2.13}$$

where μ makes reference to the mean stiffness value, subscript (1) for inclusion and (2) for background.

Accuracy:
Accuracy is the establishment of the degree of proximity of a measurement with respect to a reference value. In this particular case, between the estimated elasticity value and the tissue reference value.

$$Error = \left| \frac{Estimation - Ground\ truth}{Ground\ truth} \right| \times 100, \tag{2.14}$$

where the estimated stiffness and the mechanical measurement (ground truth) are compared.

Chapter 3

Vibro-elastography: Phantom and ex-vivo studies

3.1 Introduction

Vibro-elastography is an ultrasound-based imaging technique and a steady-state approach to elastography. Under the assumption that the pathological tissue respond differently to excitation than a healthy one, it attempts to identify the presence of abnormal masses by applying external vibration to excite the tissue. It was developed by Emre Turgay and Rob Rohling (2006).

In its first version, it was a qualitative technique. A low amplitude multi-frequency signal (< 30 Hz) was transmitted to the tissue by means of a vibrator. The displacement produced in the tissue is fitted to a parametric model or the frequency response is computed to find the relative stiffness.

At low excitation frequencies, the propagation wavelength can not be properly captured and additionally the boundary forces are unknown, whereby it is only possible to perform relative measurements. Nevertheless, increasing the frequency leads smaller shear wavelengths, allowing to capture the information of inertial forces, being feasible to perform quantitative measurements.

Increasing the excitation frequency and considering that the viscoelastic region can be modeled by a separable Helmholtz equation (ignoring out of plane variation of the displacement), Vibro-elastography became a quantitative technique, being able to reconstruct elasticity maps even in real time.

3.2 Vibro-elastography

3.2.1 Theory

In this technique, an ergonomic mechanical actuator comes into contact with the tissue surface, emitting a multi-frequency excitation that is propagated through the underlying structure. Although the induced excitation in the tissue has normal direction, shear waves continue to be generated [35].

Once the steady state wave has build-up, several RF frames are acquired to monitor the tissue displacement. In that sense, after applying speckle tracking methods in consecutive frames for each spatial position within the image, temporal series of displacement per pixel are obtained. By applying the band-pass sampling method, it is possible to reconstruct the motion at a lower sampling rate than the required by the Nyquist theorem. After passing the information to the frequency domain, the complex

phasor for each pixel $U(x,y)$ at the excitation frequency used is calculated.

It is well known that the linear elastic wave propagated related to the displacement $\mathbf{d}$ can be described in the frequency domain by Equation (3.1).

$$\nabla \cdot [\mu(\nabla \mathbf{d} + (\nabla \mathbf{d})^T + \lambda(\nabla \cdot \mathbf{d})I] = -\rho\omega^2 \mathbf{d}, \tag{3.1}$$

where λ and μ are the Lamé parameters, ρ is the density and ω is the frequency variable. Since with ultrasound only 2D information is available, it is necessary to decouple the Equation (3.1) to infer mechanical properties. This can be done through considering some assumptions. First, that soft tissue density is approximately the same as water (*i.e.*$1000\ kg/m^3$). Second, that soft tissue is considered nearly incompressible ($\nabla \cdot \mathbf{d} = 0$), which leads to consider the Poisson ratio as close to 0.5. Last, that the shear modulus can be considered as locally homogeneous, meaning that its spatial derivatives are negligible.

With the assumptions given above, the Equation (3.1) can be decoupled using the Helmholtz equation. Thus, as a result, the displacement pattern in an isotropic medium is expressed by Equation (3.2)

$$\mu \nabla^2 \mathbf{d} = -\rho\omega^2 \mathbf{d}, \tag{3.2}$$

Using the displacement phasor defined above, the same equation can be expressed as

$$\mu \left(\frac{\partial^2 U_x}{\partial x^2} + \frac{\partial^2 U_x}{\partial y^2} \right) = -\rho\omega^2 U_x, \tag{3.3}$$

Where μ is the shear modulus. Using the second assumptions, it follows that

$$E = 2\mu(1+\nu) \approx 3\mu, \tag{3.4}$$

Finally, the local shear speed can be estimated by using a Local Frequency Estimator (LFE) for solving the Helmholtz equation, what allows to infer the elasticity value for each point in the region of interest (ROI). From a serie of elastograms obtained while the vibration is exerted, a single one is computed by averaging the results for each frequency emitted.

3.2.2 Vibro-elastography system

The elastographic driver box (Clarison Medical, British Columbia, Canada) is a module that has the capability to produce two elastography techniques: Vibro-elastography and Crawling Waves. It has a built-in signal generator, that is driven by a graphic interface. The equipment is connected to a SonixTouch system (Ultrasonix, British Columbia, Canada), with which it communicates through a Porta API, obtaining access to the imaging "engine backend". The main advantage is the capability to access to the clinical B-mode image, while the disadvantage is the lack of scanner control (i.e. sequence parameters). An actuator connected to the driver box contains two small shakers, which emit vibration depending on the selected mode: Vibro-elastography or Crawling Waves. A linear array ultrasound transducer (L14-5, Ultrasonix, British Columbia, Canada) was coupled to the actuator, which in turn was attached to a metallic plane plate that came into contact with the tissue. Then, plane waves were emitted. The general experimental setup used for data acquisition can be seen in Figure 3.1.

Besides visualizing the elasticity map in real time, data files can be saved in order to perform offline processing.

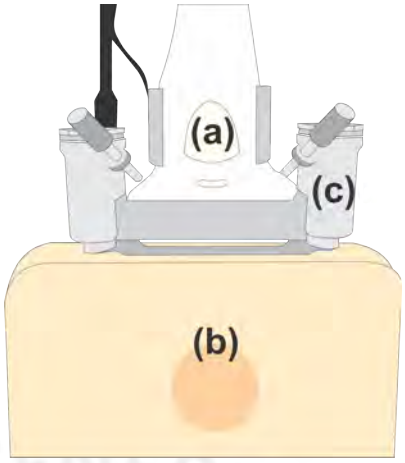

Figure 3.1: Experimental scheme used for Vibro-elastography. (**a**) Transducer, (**b**) sample or tissue and (**c**) actuator that contains two small shakers and a metallic plane plate in contact with the tissue.

3.2.3 Single and multi-frequency excitation

Vibro-elastography images were acquired after inducing propagation in the soft tissue using an external excitation, whether of a single frequency or multi-frequency. The algorithm of Vibro-elastography processing is based on making data fitting corresponding to a certain frequency. Evidently, if more data is available, a greater number of equations will be used to make a more optimal fitting. In the case where a multi-frequency signal is used, its components must be considered close to each other to avoid dispersion when estimating the elasticity.

3.3 Phantom experiments

3.3.1 Phantom: manufacturer specification

In order to evaluate the accuracy and repeatability of the measurements, elastograms were acquired by applying the technique on a calibrated breast elastography phantom (Zerdine model 059, CIRS, Virginia , USA).

According to the manufacturer, the phantom mimics the ultrasonic characteristics, the size and the shape of an average breast from a person in supine position. The phantom contains many small inclusions randomly located, which appear hypoechoic and their size range between 3 to 10 mm.

The manufacturer has reported that the background has an elasticity of 20 $\pm$ 5 KPa, while the small masses have at least twice the elasticity value of the background. In that sense, it is reasonable to consider inclusion stiffness as 50 KPa. Single-frequency signals were applied to the surface of the phantom, in the interval between 170-240 Hz in steps of 10 Hz. For each frequency selected, the acquisition was repeated 4 times (each one in a different day), to verify repeatability.

Figure 3.2: Calibrated breast phantom used for experiments.

3.3.2 Phantom: gelatin-based specification

A gelatin-based phantom with a cylindrical inclusion of 15mm diameter was used for experiments, which had a 8% of gelatin concentration in the background and 15% of gelatin concentration in the inclusion. It was elaborated by a mixture of 69.5g and 141.2g gelatin for 8% and 15% respectively, 7.2g of NaCl, 12g of agar and 16g of cornstarch. The ingredients were mixed in 800 mL of water at 100°C, then was cooled to 35°C. Finally, the mixture was then poured into a plastic box of $13 \times 13 \times 9$ cm^3, stored in the fridge and left overnight.

Following the scheme presented in figure 2.2, experiments to find a reference value were carried out. The shear speed for the background was 3.47 m/s, while for the inclusion was 4.7 m/s. Expressed in KPa, the reference value was 36.28 KPa for background stiffness and 66.27 KPa for inclusion stiffness.

3.3.3 Results

Calibrated breast phantom

As stated previously, Vibro-elastography was tested several times on a calibrated breast phantom using a range of frequencies from 170 to 240 Hz, in order to evaluate its performance and the repeatability of its measurements. Some results are shown in Figure 3.3.

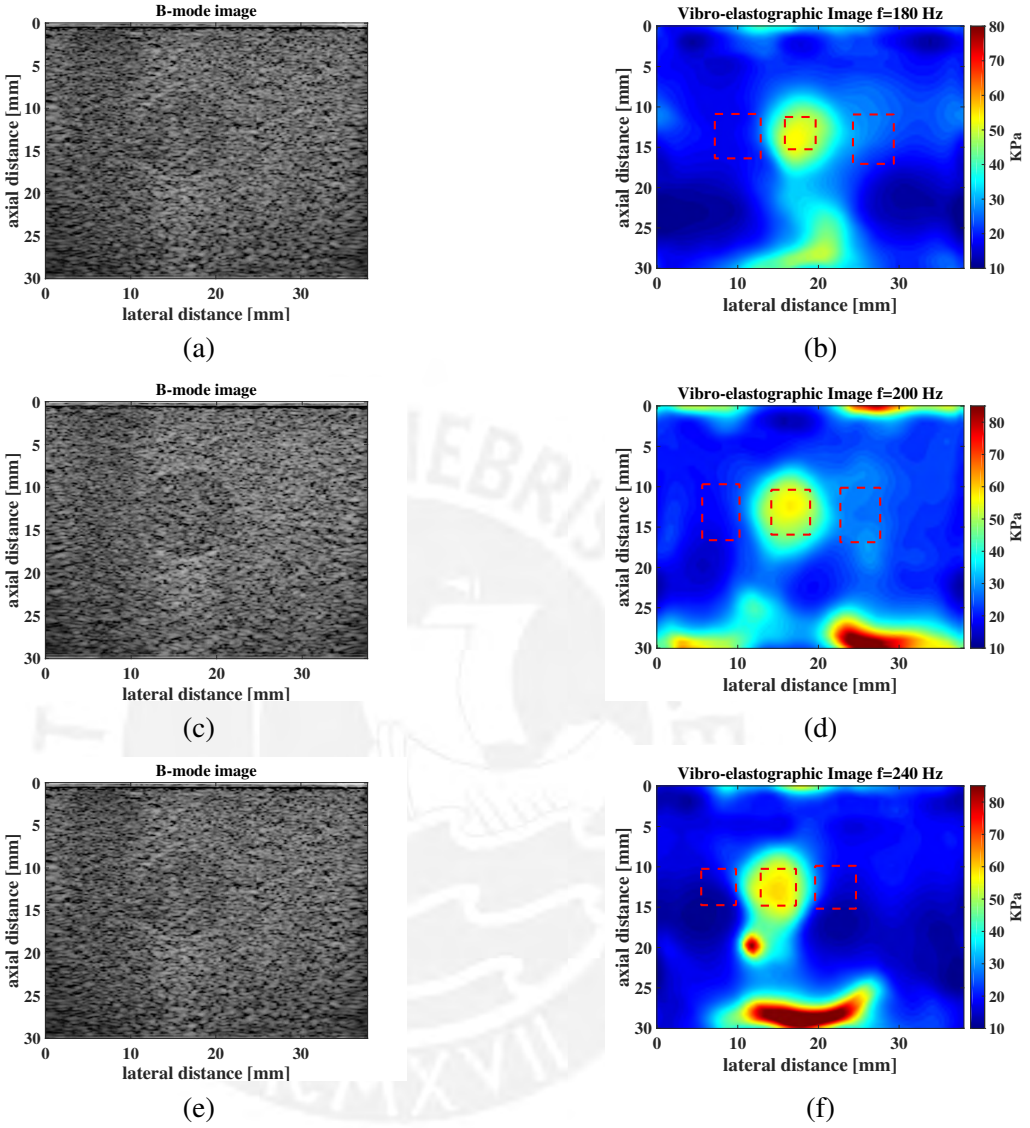

Figure 3.3: (a), (c) and (e) are B-mode images from the calibrated breast phantom. Images (b), (d) and (f) are elasticity maps obtained at frequencies of 180 Hz, 200 Hz and 240 Hz, respectively.

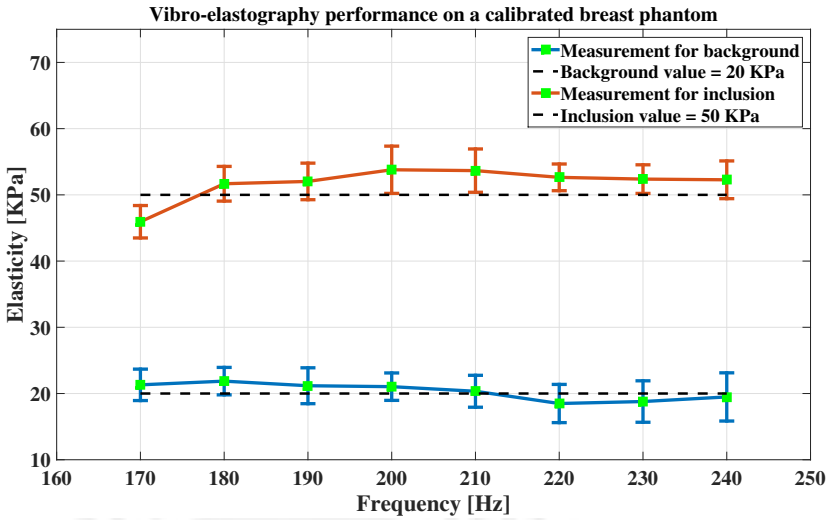

Figure 3.4: Estimation performed by Vibro-elastography as the excitation frequency increases. For each frequency, the estimated value presented corresponds to an average of four measurements (one for each day).

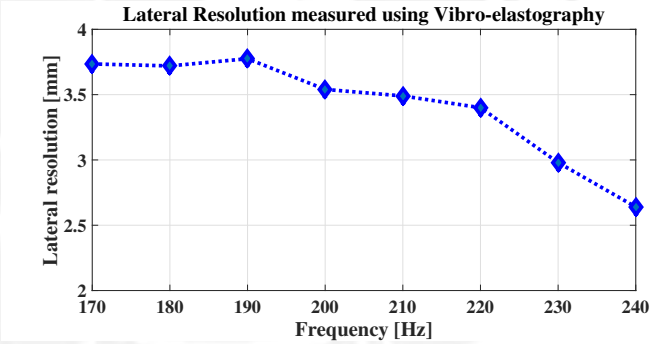

Figure 3.5: Lateral resolution value vs excitation frequency for a calibrated breast phantom.

The Vibro-elastography measurements as the frequency increases are presented in Figure 3.4. Elasticity measurements have shown a good agreement with the values reported by the manufacturer. For the background, the maximum relative error obtained is 7.2%, being the mean error 4.96%. In the case of the inclusion, the maximum error is 10% (produced at 170 Hz), while the mean error is 3.56%. Additionally, since the standard deviations for the whole range of frequencies used are low and the experiments were performed at different times, repeatability has been proven.

The metrics evaluation is summarized in the table 3.1.

Table 3.1: Metrics obtained by analizing a calibrated breast phantom.

Metric	Frequency (Hz)							
	170	180	190	200	210	220	230	240
Background stiffness	21.31	21.87	21.18	21.04	20.34	18.49	18.79	19.48
Inclusion stiffness	45.94	51.68	52.03	53.79	53.66	52.65	52.38	52.27
Lateral resolution	3.74	3.72	3.78	3.54	3.49	3.40	2.98	2.64
Contrast	1.16	1.30	1.49	1.44	1.56	1.86	1.97	2.27
CNR	7.15	9.12	7.95	8.87	9.16	9.64	8.52	8.25
SNR background	18.25	19.46	17.80	22.07	18.14	16.12	15.74	12.11
SNR inclusion	26.05	27.69	25.67	24.93	27.49	28.47	29.20	28.72

Gelatin-based phantom

With the intention of confirming the trend and the metrics obtained with the calibrated phantom, it was decided to make a new series of experiments, but this time in a phantom made with gelatin. Following a procedure similar to that used for the calibrated phantom, estimates of elasticity of both the inclusion and the background were made in a frequency range from 100 to 300 Hz. The Vibro-elastography

Table 3.2: Metrics obtained by analizing a gelatin-based phantom.

Metric	Frequency (Hz)							
	100	130	160	190	220	240	270	300
Background stiffness	35.77	36.84	36.79	36.61	30.72	35.49	36.08	32.01
Inclusion stiffness	70.14	62.51	63.72	66.02	69.35	62.39	61.27	62.78
Lateral resolution	5.47	5.04	4.79	3.88	3.43	3.75	2.95	2.17
Contrast	0.96	0.70	0.73	0.80	1.25	0.75	0.69	0.96
CNR	5.43	5.21	6.16	8.69	5.55	5.58	5.79	6.28
SNR background	18.25	19.46	17.80	21.55	19.04	19.18	23.95	21.63
SNR inclusion	24.38	21.54	25.24	28.93	23.00	25.65	21.06	22.69

measurements as the frequency increases are presented in Figure 3.7 for a wide range, between 100 - 300 Hz. Elasticity measurements are in agreement with the reference values obtained through the time of flight experiment. For the background, the maximum relative error obtained is 15.32% and the mean error 3.42%. In the case of the inclusion, the maximum error is 5.86%, while the mean error is 2.25%. The metrics evaluation is summarized in the table 3.2.

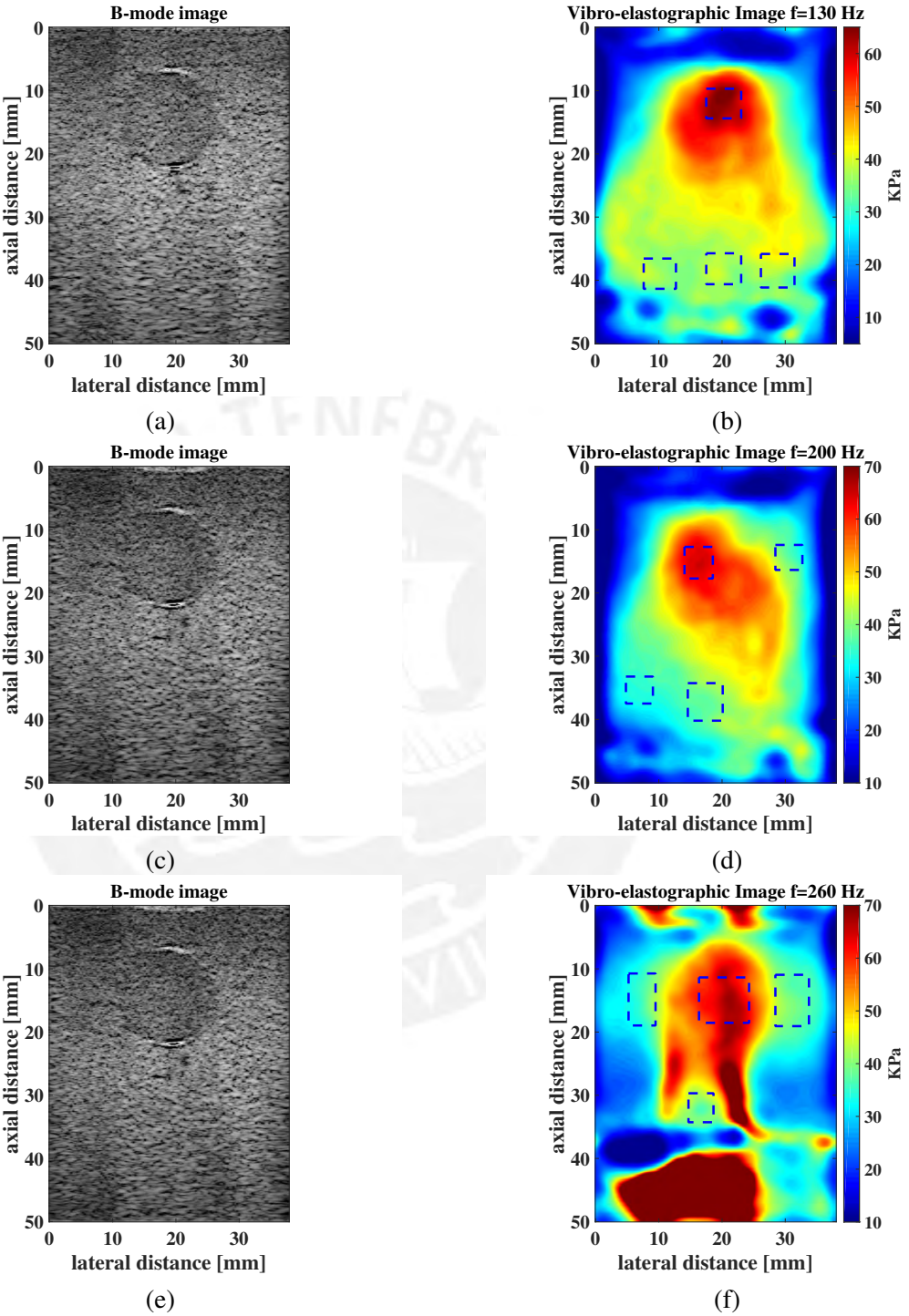

Figure 3.6: (a), (c) and (e) B-mode images from a gelatin-based phantom. Images (b), (d) and (f) are elasticity maps obtained at frequencies of 130 Hz, 200 Hz and 260 Hz, respectively.

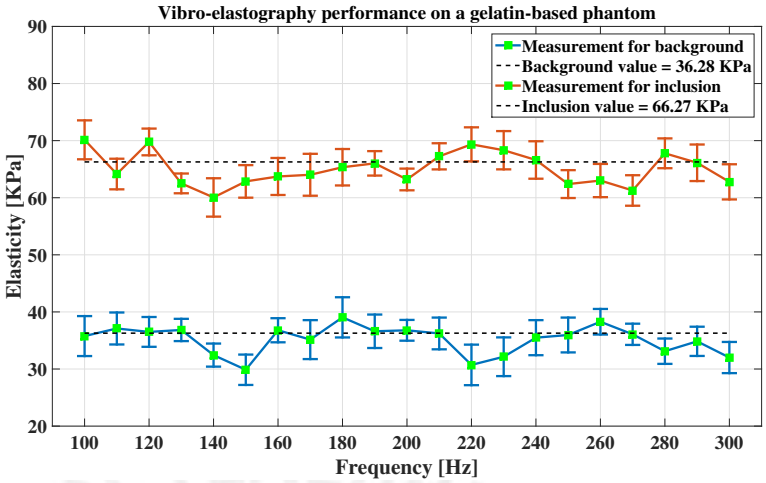

Figure 3.7: Elasticity estimation using Vibro-elastography as the excitation frequency changes.

3.4 Ex-vivo experiments

In an attempt to go further, excised pig kidney was selected to perform experiments on ex-vivo tissue. There are some reasons for this selection. First, scientist in recent years are showing interest in animal organs to conduct cross-species organ transplant, in particular porcine kidney since it has potential for successful transplant. Second, the homogeneity of the surface layer of the organ, which makes feasible its analysis using elastography since there are no internal structures that can be a source of undesired reflections or artifacts. Last, it is relatively simple to obtain fresh pig kidney samples.

3.4.1 Sample harvest and preservation

The freshly excised pig kidney sample was conditioned in a recipient with a saline solution on its walls, to prevent dehydration of the organ. To avoid drastic changes in the mechanical properties of the kidney, the experiments were performed in less than 12 hours after harvested.

Prior to the experiments, a brief perfusion process was performed to remove possible blood residues in internal ducts.

Figure 3.8: Perfusion procedure for an ex-vivo pig kidney.

3.4.2 Data acquisition

Following the same procedure used for phantom experiments, a similar experimental setup was used, as is shown in Figure 3.9.

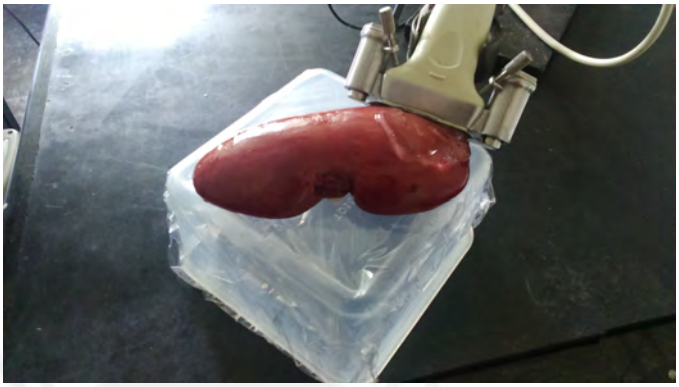

Figure 3.9: Data acquisition stage for an ex-vivo pig kidney.

Schneider *et al*. [36] performed a similar experiment, where porcine kidney samples were analyzed for frequencies between 50 to 175 Hz. After analyzing the stiffness values obtained, it was concluded that as the frequency increases, an intrinsic viscous component appears, which causes the increase of the elasticity value. The frequency range that practically remains unaffected corresponds to frequencies less than 100 Hz. For this reason, it has been chosen to work with a multi-frequency signal f=[80 90 100], working at low depth since the region of interest was only the cortex.

3.4.3 Results

Three different pig kidney samples were tested at different days, which were conserved properly after harvested. Results are shown in Figure 3.10.

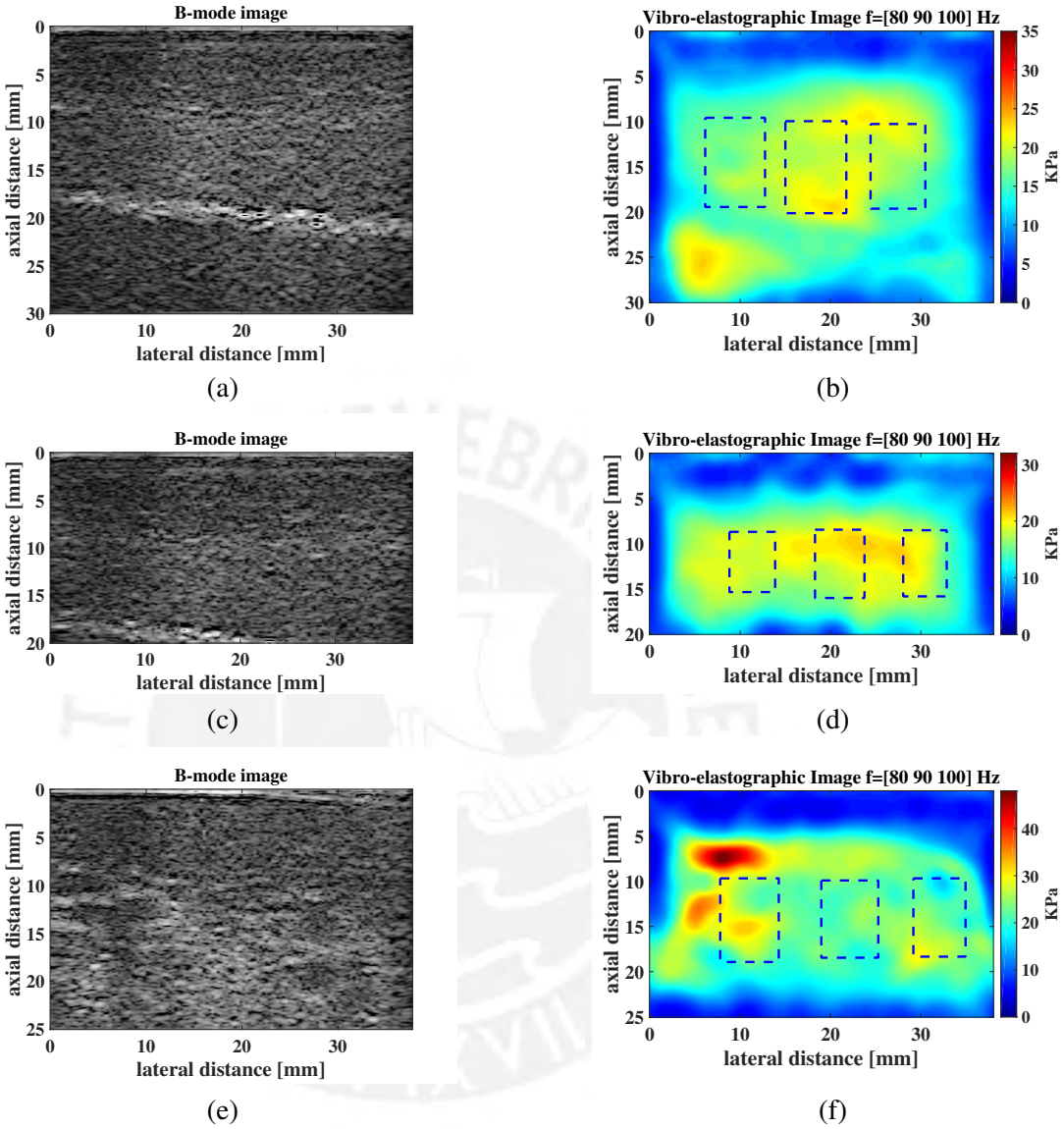

Figure 3.10: B-mode (left) and elasticity map (right) for $f = [80\ \ 90\ \ 100]$ Hz for sample 1 (a and b), sample 2 (c and d) and sample 3 (e and f) respectively.

From all the experiments, the mean value obtained was 20.4 ± 1.5 KPa.

3.5 Discussion

From the summary table 3.1 and 3.2, it can be seen that the elasticity measurements suggest consistent behavior by the Vibro-elastography technique. Background elasticity estimates as well as inclusion elasticity estimates for both calibrated and gelatin-based phantom are pretty close to the expected value, even when the excitation frequency changes.

As the frequency increases, a lower lateral resolution is expected, since the shear wavelengths must be progressively reduced. According to the results obtained, Vibro-elastography presents a coher-

ent lateral resolution trend, starting at 3.74 mm and yielding a final value of 2.64 mm for the calibrated phantom in a [170-240] Hz range, and starting at 5.47 mm and yielding a final value of 2.17 mm for the gelatin-based phantom in a [100-300] Hz range.

It is possible to compare the results with those reported for other elastographic techniques. Ormachea [37] reported lateral resolution measurements for Crawling Waves (obtained through the Phase Derivative estimator) in a range between 220 - 500 Hz, which presents a lateral resolution of [2.48 - 4.19] mm. Lateral resolution values for STL-ARFI in the same frequency range were reported, which ranged from 2.45 mm to 4.15 mm. Then, results suggest that Vibro-elastography has a similar behavior than these techniques, even achieving a better lateral resolution for certain frequency points.

Given the values reported by the manufacturer and considering that the lesion stiffness is 50 KPa, the expected contrast lies in the range of $[1-2.3]$. The estimates show values that are within that range. In the same way, for the gelatin-based phantom it was expected to obtain a contrast of 0.82, a value with which the measurements agree. Roughly, CNR and SNR present a stable trend in the range covered. Specifically, CNR values obtained in this study agree with the reported by Mahdavi *et al*. [39].

Additionally, ex-vivo experiments were carried out on pig kidney. The superficial 20 mm of the organ were of interest for this study, since it exhibited homogeneity. Elastograms were obtained for each sample, calculating a mean stiffness value that agrees with the study carried out by Schneider *et al*. [36], who reported a elasticity of 21 ± 3KPa at 0 mmHg of internal pressure in the kidney. Good images were acquired for the set of frequencies specified. For this reason, similar frequencies were selected to perform in-vivo measurements.

Chapter 4

Vibro-elastography: Clinical studies

4.1 Introduction

In the previous chapter, in order to evaluate the accuracy and repeatability of the Vibro-elastography technique estimates, elastograms were acquired from a calibrated breast elastography phantom (Zerdine model 059) and from an ex-vivo organ. In this chapter, the technique was used to perform clinical tests, attempting to evaluate its diagnostic capability.

4.2 Patient data collection

Participants signed an informed consent approved by the International Review Board of the Universidad de San Martín de Porres. In total, 18 patients were enrolled in this study. The data acquisition was performed before biopsy by a radiologist at Oncosalud – Auna according to standard protocols. The elastography images were obtained using a multi-frequency signal with components of $80, 90$ and 100 Hz, being cautious when selecting the frame rate (35 Hz for this case), which yields the frequency components at $10 - 15 - 5$ Hz in the baseband. A radiologist was in charge of the location of the lesion in the B-mode image, holding the probe as firmly as possible. The first 20 seconds after turning on the mechanical excitation were intended to allow the shear wave propagation to build up. Then, the elastographic data was saved. It is worth noting that both the B-mode and the elastographic images were acquired at the same plane and at the same depth. Later, the patient was transferred to another room where the same radiologist performed the biopsy. One biopsy core per patient was taken.
The elastograms were posteriorly compared with the histopathological findings, which made it feasible to evaluate Vibro-elastography performance in clinical application.

4.3 Patient results

The data acquired in the Health Center was processed offline to produce quantitative elastograms. Regions of interest (ROI) inside the lesion and the surrounding tissue were selected to calculate mean stiffness values. In general, the excitation frequencies used are $80, 90$ and 100 Hz. Some results can be seen in Figure 4.1, where the B-mode and elastograms are presented. The results for the 18 patients are presented in the annex.

The histopathological findings indicated that 6 patients presented a malignant lesion, while 12 presented benign ones. Among the benign lesions, 3 of them were fibroadenomas, 3 were adenoids

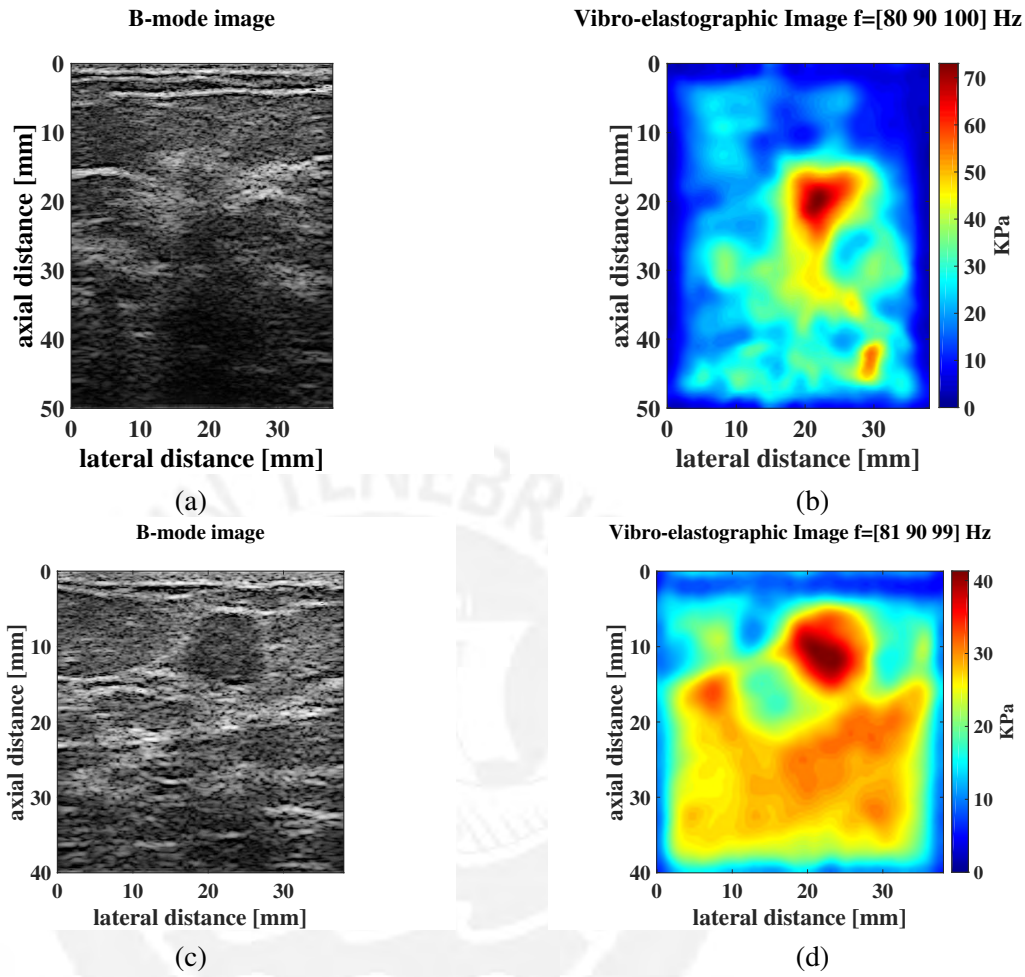

Figure 4.1: B-mode of a patient breast presenting a solid lesion (a) and (c), and their corresponding elastographic map (b) and (d).

(ductal and nodular), 4 were papillary lesions, one was fibroepithelial lesion and the last was lymphoid tissue. A classification between benign and malignant cancer was performed according the biopsy results and the elasticity values estimated. For this, SVM (Support Vector Machine) was used. The lesion stiffness measurement and the ratio between the lesion and the background stiffness were used for data classification, which is presented in Figure 4.2.

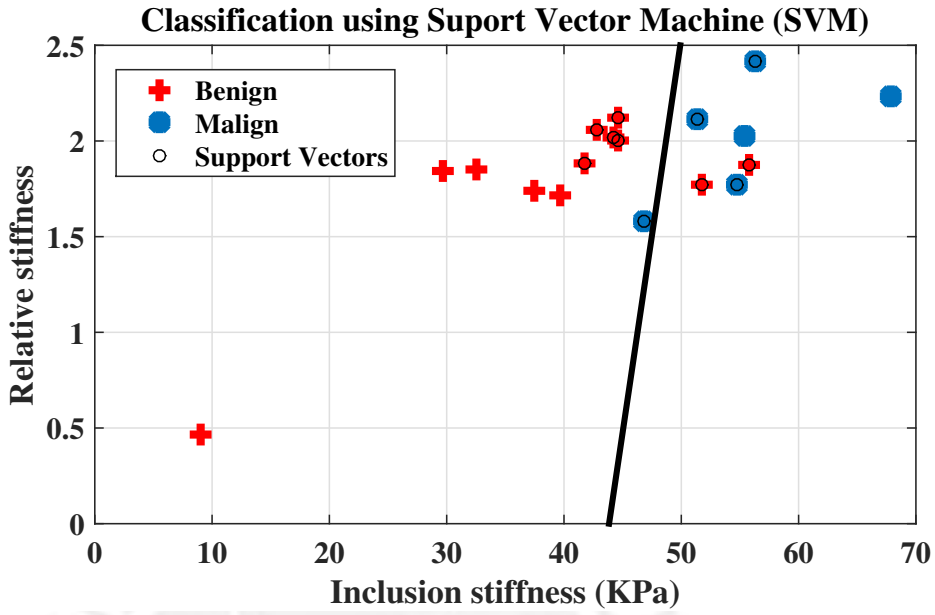

Figure 4.2: Classification of results obtained with Vibro-elastography, using SVM.

4.4 Discussion

Vibro-elastography was used for breast characterization in clinical cases. As could be seen in the presented elastograms, the elasticity images in general permitted to distinguish the lesion from the breast parenchyma in a good degree. However, in many cases the contrast of the lesion with respect to the surrounding healthy tissue did not allow to identify clearly between cases of benign and malignant cancer. This can be attributed to the histopathological findings. None of the malignant cases were of a high histopathological degree (at most they were intermediate). In addition, it is known that most patients come to the clinic affiliated to the study to perform cancer screening, but not treatment of the disease. In this way, the possibility of finding cases of cancer in late stage (which means in turn high stiffness values for the lesion) is almost null.

A curious case is that corresponding to an isolated point in the diagram (inclusion stiffness of 10 KPa and ratio of 0.5). This is not exactly a lesion, but a ductal dilatation case, caused by the obstruction of ducts through which the milk flows during the lactation stage.

There are studies that have also used elastographic techniques to classify benign and malignant breast lesions. Eskandari [40] performed a study using vibro-elastography for this purpose in a dataset of 20 patients. Olgun [41] used shear wave elastography, calculating values of minimum, maximum and average elasticity in each case, as well as a cut off value. Evans [42] also used shear wave elastography, but supported the BI-RADS classification of ultrasound imaging. All these results are shown in the table 4.1.

Table 4.1: Mean elasticity values for benign and malignant cancer according literature.

Technique	Elasticity (KPa)		
	Cut off value	*Benign lesion*	*Malignant lesion*
Vibro-elastography [40]	-	23	42
Shear wave elastography [41]	-	25.25	156.66
Shear wave elastography [42]	50	40	153
Supersonic shear imaging [16]	-	45.3	146.6
Comb-push Ultrasound SE [43]	-	30.18	90.66

The results encourage to evaluate a larger cohort of women with patients at advanced disease, to get an improved assess of the goodness of the technique.

Chapter 5

Normal Vibration Holography

5.1 Introduction

Wu *et al*. [30] proposed an experimental arrangement formed by two shakers which - using US Doppler variance - allowed to generate and analyze a slow motion interference pattern termed crawling waves. After examining its propagation over a region of interest (ROI), it is possible to measure the shear wave speed in the medium.

Nonetheless, the requirement of placing two aligned vibrators facing one to each other results impractical in most clinical cases. Therefore, Wu *et al*. [30] presented a new technique named Shear Wave Holography, which uses holography to form a dynamic interference pattern. The shear wave speed is estimated using the same analysis performed for Crawling Waves. However, in its configuration the vibrator is not coupled to the probe, and both are required to move periodically with a slight difference in frequency between them, what makes its application impractical.

In that sense, a new experimental scheme that produces a static interference pattern by using holography is proposed, where a small indenter producing normal vibration is introduced -instead of a lateral one-, while also induces a harmonic motion in the probe.

5.2 Normal Vibration Holography

5.2.1 Theory

The Shear Wave Holography technique is based on adding effects from a point source acting on the surface inducing shear waves in the tissue and from the probe, which must vibrate in a harmonic fashion and acts as the frame of reference. Both, the shear wave source and the probe motion are described by (5.1) and (5.2) respectively.

$$U(r,t) = \frac{B}{r} e^{\omega t - k_s r}, \tag{5.1}$$

$$R(t) = A e^{i\omega t}, \tag{5.2}$$

where r is the radial variable, t is the time variable, A and B are the vibration amplitudes, ω is the angular frequency and k_s is the wave number. Since both vibrated at the same frequency, a static interference pattern over the time was obtained. Using a simple relation for relative motion, the vibration field respect to the probe is given by (5.3)

$$P(r,t) = U(r,t) - P(t), \tag{5.3}$$

Since sonoelastography describes the amplitude of the vibration field, Equation (5.3) is multiplied by its complex conjugate. Then, after replacing Equation (5.1) into Equation (5.2), it is obtained

$$|P(r,t)|^2 = \frac{B^2}{r^2} + A^2 - \frac{2AB}{r}\cos(k_s r), \tag{5.4}$$

5.2.2 Experimental setup

The equipment required were a small voice coil -which is the shear wave emisor-, a SonixTouch Research System with a linear array (L14-5) ultrasound probe (Ultrasonix, British Columbia, Canada). The probe and the voice coil were attached to an ergonomic case, which makes easier the mechanical coupling, while favoring the probe to adopt the same frequency vibration than the voice coil, as shown in Figure 5.1. In that sense, when the case was used to examine the soft tissue, a static interference pattern was produced.

Given that the voice coil is placed on the top of the tissue, a normal vibration will be applied. Despite

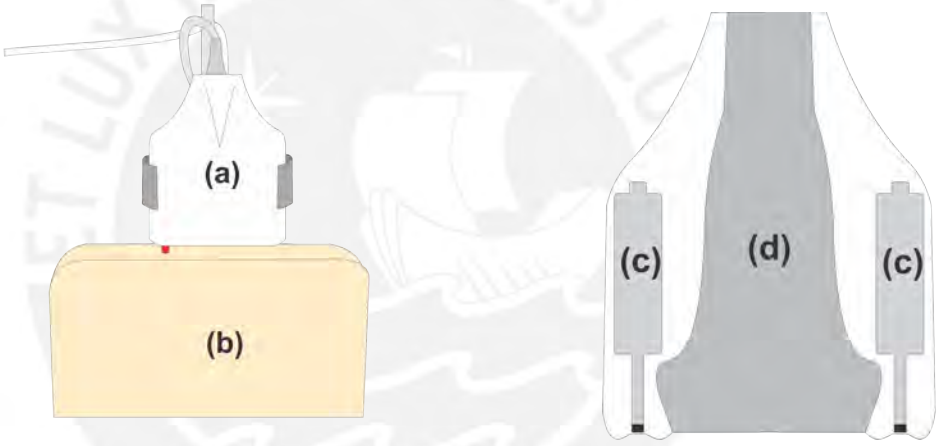

(a) (b)

Figure 5.1: (a) Experimental setup for holographic interference pattern formation: (**a**) case containing the probe and the voice coil and (**b**) tissue-mimicking phantom. (b) a detailed representation of the case: (**c**) compartment for the voice coil and (**d**) for the probe.

its longitudinal nature, shear waves will be generated, since elastic waves at the boundary of two media will produce a reflection and refraction of compressional and shear waves [35].

5.2.3 Phase Derivative algorithm

The speed estimation process was performed based on the Phase Derivative algorithm. Its derivation begins after discretizing the Equation (5.4).

$$s(m,t') = \frac{B^2}{r^2} + A^2 - \frac{2AB}{m}\cos(k_s m T_m), \tag{5.5}$$

where m is the discrete representation for the radial variable, t' for the time and T_m denotes the spatial sampling interval in the shear wave propagation direction.

According to the Phase Derivative algorithm, the local shear speed can be estimated by computing the spatial derivative of the phase term corresponding to the discrete pattern expression stated in (5.5).

$$\frac{\partial \phi}{\partial m} = \frac{\partial (k_s m T_m)}{\partial m} = k_s T m, \tag{5.6}$$

Given that $k_s = {}^{2\pi f_s}/_{c_s}$, and rearranging terms, the shear speed is expressed by

$$c_s = \frac{2\pi f_s}{\theta'}, \tag{5.7}$$

being f_s the vibration frequency and θ' the phase derivative term.

5.2.4 Algorithm for speed map estimation

As can be seen in Figure 5.3, a radial interference pattern was produced, which was static over the time. Thus, only one frame was available for analysis. First, a denoising stage was performed, which consisted on media filtering and contrast enhancement. Then, the 2D speed estimation task was separated into several 1D tasks, working on the propagation direction. For this purpose, the voice coil position was considered as the origin of the propagation. Then, a point with coordinates (x, y) was selected, and a straight line connecting it with the origin was traced. Using this line, a profile from the pattern image was extracted, which had to be a sinusoidal curve representing the amplitude vibration in that specific radial direction. Finally, the shear speed was estimated by applying Equation (5.7). The process was repeated for several points within the region, after which a partially constructed speed map was obtained. Interpolation is used to fill the empty areas.

5.3 Simulations

The objective was to simulate the interference pattern formation in homogeneous and heterogeneous media, as should be obtained when applying the experimental scheme described previously. To achieve this, the k-wave toolbox [44] and Matlab (MATLAB 8.0 and Statistics Toolbox 8.1, The MathWorks, Inc., Natick, Massachusetts, United States) were used. The simulations were performed for a region of interest of 50×50 *mm*, where the medium density is 1000 ${}^{kg}/_{m^3}$. The interference pattern was formed by the action of a point source oscillating at a frequency f (where $f \in [200, 300, 400]$ Hz) with a strength of 10^6 Pa, while a sensor is recording the phenomena. The selected medium speed for simulations were 2, 3, 4 and 6.5 m/s. To avoid reflections at the grid boundary, a perfectly matched layer is set around it. The shear speed was established by setting the propagation speed in the medium. Finally, to get a more realistic interference pattern, Gaussian noise was added (μ=0, σ=0.01).

5.4 Phantom experiments

Two gelatin-based phantoms were manufactured for experiments: one homogeneous and the other heterogeneous. The homogeneous one was prepared by a mixture of 69.5g of gelatin, 7.2g of NaCl, 1.2g of agar and 16g of cornstarch, which were mixed in 800 mL of water at 100°C. The heterogeneous phantom was manufactured in two stages: one for the background and the other for the inclusion. The background was elaborated with 218.18g of gelatin, 7.2g of NaCl, 1.2g of agar and 32g of cornstarch in 1600 mL of water; while the inclusion was elaborated with 114g of gelatin, 5.4g of NaCl, 1.2g of agar

and 12g of cornstarch in 600 mL of water. In both cases, after the mixture was heated to 100°C, it had to wait until its temperature dropped to 35°C. Finally, the mixture was then poured into a plastic box, stored in the fridge and left overnight. When the phantom was ready to use, it was examined using the experimental scheme presented in Figure 5.1. The homogeneous phantom was analyzed at frequencies ranging from 250 Hz to 300 Hz in steps of 10 Hz. In contrast, for the heterogeneous phantom another procedure was chosen, which consisted on analyzing it by means of a sweep of frequencies around a central frequency. This is because when producing a static interference pattern, certain regions inside the phantom will not vibrate, which can cause small lesions not to be detected. Thus, in order to avoid the presence of artifacts due to the analysis of a static pattern, it is feasible to work with a small range of excitation frequencies (in particular 296-304 Hz) in steps of 2 Hz. This will allow to excite every part inside the medium. Since the frequencies belong to a small neighborhood in the frequency domain, speed dispersion can be disregarded.

5.4.1 Shear speed from mechanical measurements

Homogeneous phantom

The mean speed for all the speed maps gave a value of 2.52 m/s. Given that the value of reference is 2.64 m/s, the mean relative error of estimation is 4.6%, and the maximum error is 6% (at 260 Hz, where the mean speed is 2.48 m/s).

Heterogeneous phantom

The mechanical tests were performed in the CITE - Materiales PUCP laboratory with two samples of $3 \times 3 \times 3$ cm. The compression rate and the strain value were adjusted to 0.5 mm/s and 5%, respectively. Test lasted about 700 s. The stress relaxation curve of each sample during the period was fitted to a KVFD model using MATLAB curve fitting toolkit.

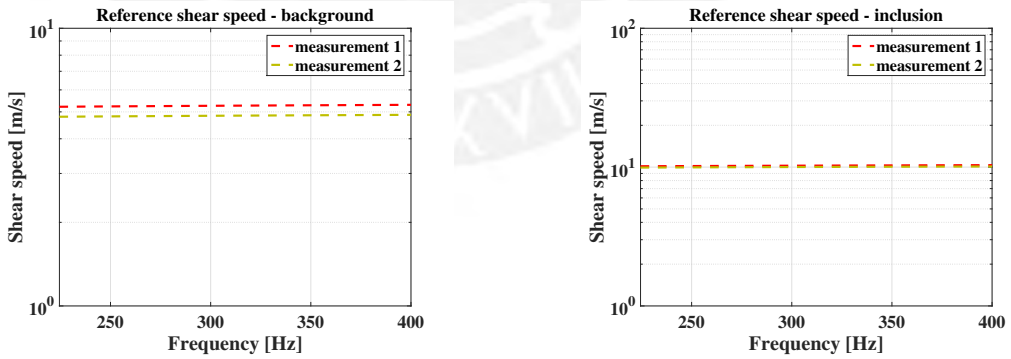

(a) (b)

Figure 5.2: (a) Shear speed estimation using mechanical measurements for the background as a function of frequency, (b) Shear speed estimation using mechanical measurements for the inclusion as a function of frequency

For the background, the mean shear speed value computed from the measurements was 5.01 m/s, while for the background was 10.04 m/s. Shear speed estimation as a function of frequency for both cases can be seen in Figure 5.2

5.5 Results

5.5.1 Simulation results

As stated before, simulations were performed for a variety of conditions. The results are presented in table 5.1.

Table 5.1: Speed estimation for different vibration frequency and simulated media speed

Frequency (Hz)		m/s			
	Medium speed	2.0	3.0	4.0	6.5
200	Estimated speed	1.98	2.92	3.88	6.22
	Relative error %	1	2.67	3	4.3
300	Estimated speed	2.05	2.95	3.89	6.32
	Relative error %	2.5	1.67	2.75	2.77
400	Estimated speed	2.09	3.01	3.93	6.37
	Relative error %	4.5	0.5	1.75	2

From the simulated interference patterns, speed maps were generated by applying the estimation algorithm described before. From adequate regions inside each medium, the mean value was computed for a later comparison with the speed value defined for simulation in each case.

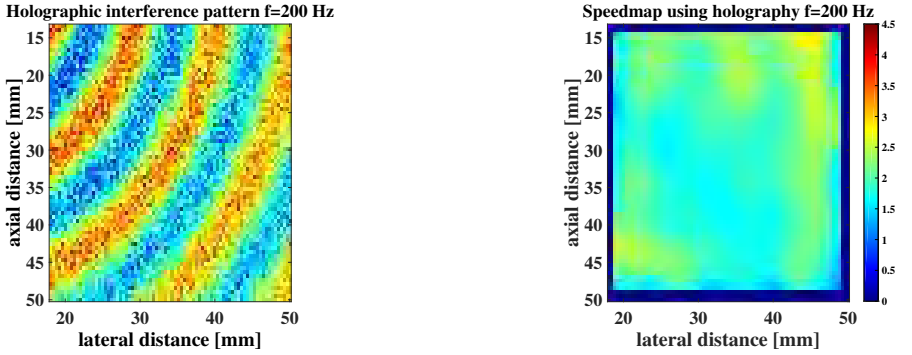

(a) (b)

Figure 5.3: (a) Simulated interference pattern using a source of 200 Hz in a homogeneous medium of shear speed of 2 m/s . (b) Corresponding speed map, where the estimated speed is 1.98 m/s

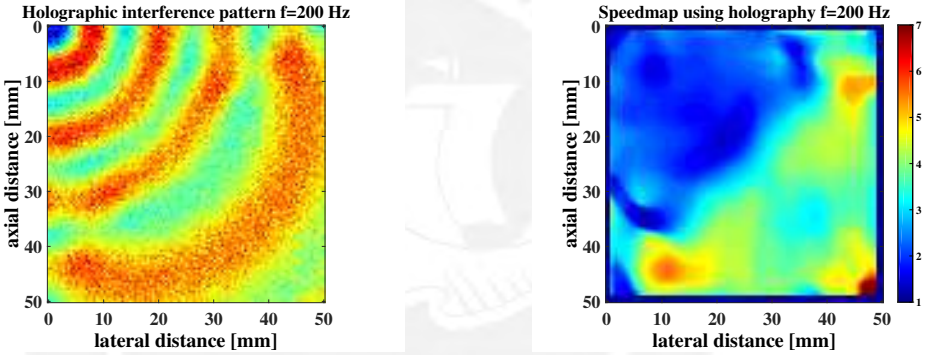

(a) (b)

Figure 5.4: (a) Simulated interference pattern using a source of 200 Hz in a heterogeneous medium. Region I has 2 m/s, while region II has 4 m/s. (b) Corresponding speed map, where the estimated speed for region I is 2.13 m/s and for region II is 3.57 m/s

The estimated results for the simulated media show a good agreement with the speed values defined when simulating the interference pattern in each case. The maximum accuracy error was 4.5%.

5.5.2 Phantom results

Homogeneous phantom

For the homogeneous phantom, at each frequency specified previously (250 Hz to 300 Hz in steps of 10 Hz), a speed map was generated. In Figure 5.5 can be seen the results for frequencies at 260 Hz and 280 Hz. The mean speed for all the speed maps gave a value of 2.52 m/s. Given that the value of reference was 2.64 m/s, the mean relative error of estimation was 4.6%, and the maximum error was 6% (at 260 Hz, where the mean speed was 2.48 m/s).

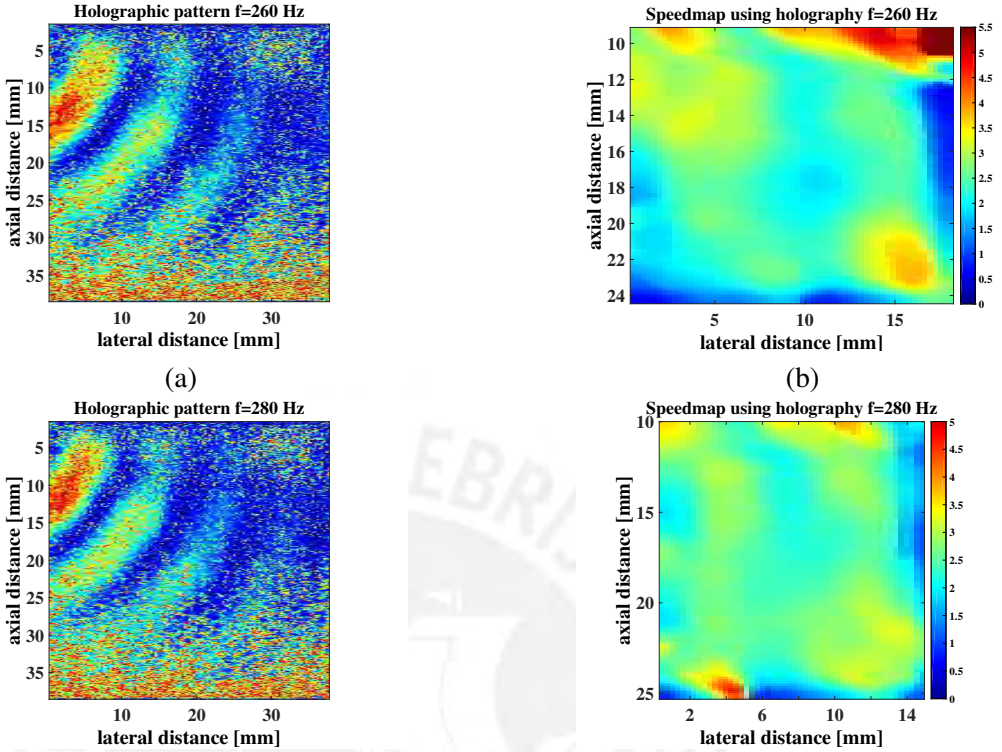

Figure 5.5: (a) Experimental interference pattern generated at a frequency vibration of 260 Hz . (c) Experimental interference pattern generated at a frequency vibration of 280 Hz. (b)-(d) Speed maps obtained at frequencies of 260 Hz and 280 Hz respectively.

Heterogeneous phantom

Using frequencies lying in a narrow-band domain (296-304 Hz in steps of 2 Hz), the heterogeneous phantom was excited. In each frequency used, the lesion remained at the same location, which in the end allowed to average the estimates obtained. Results are shown in Figure 5.6.

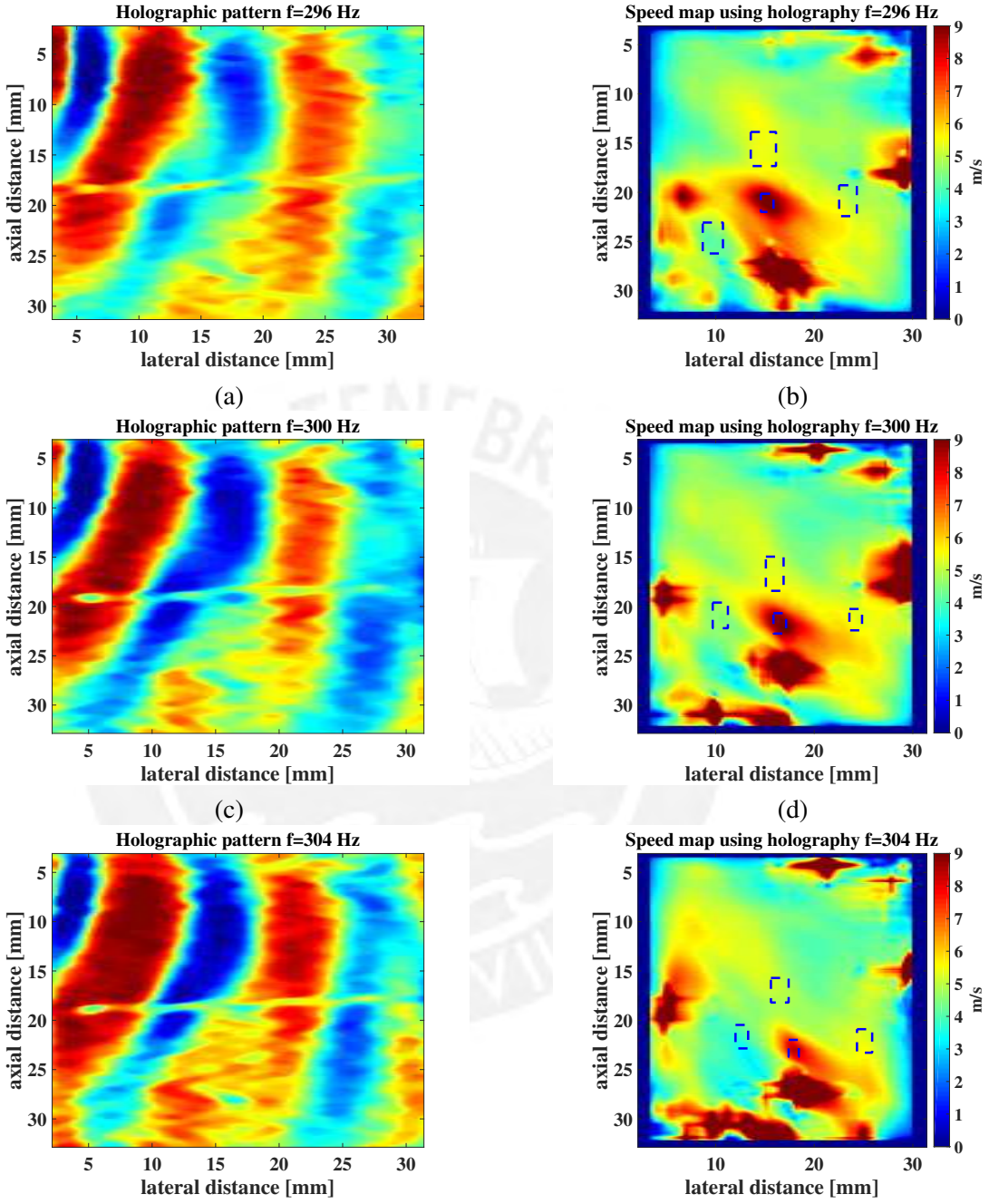

Figure 5.6: (a) Interference pattern and (b) shear speed map for f=296 Hz . (c) Interference pattern and (d) shear speed map for f=300 Hz. (e) Interference pattern and (f) shear speed map for f=304 Hz

Results show consistency between 296 – 300 Hz, out of this range the quality of the estimation decrease. Then, averaging these results, the elastogram shown in Figure 5.7 was obtained.

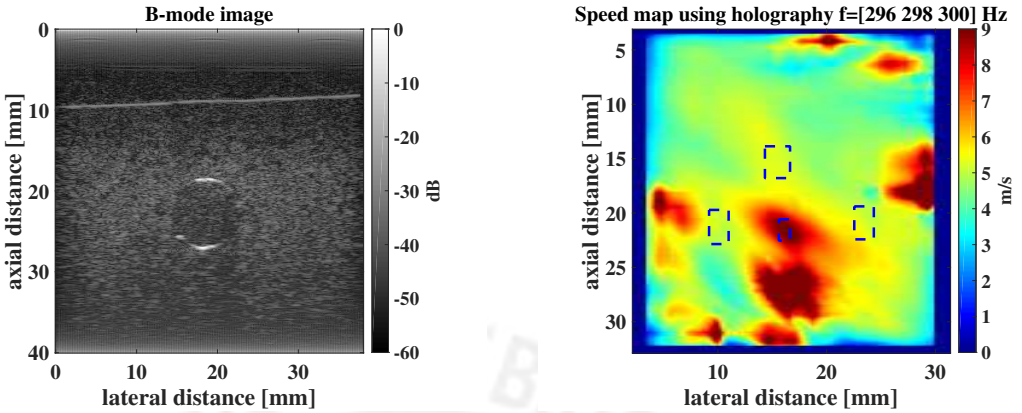

(a) (b)

Figure 5.7: (a) Bmode image corresponding to the heterogeneous phantom. (b) Speed map obtained by averaging results from single frequencies.

Additionally, estimates for each frequency used are summarized in table 5.2.

Table 5.2: Speed estimation for different vibration frequency using a gelatin-based phantom

Frequency (Hz)	Estimated shear speed (m/s)				
	296	298	300	302	304
Background stiffness	4.91 ± 0.21	5.20 ± 0.11	5.10 ± 0.15	4.96 ± 0.14	4.70 ± 0.17
Inclusion stiffness	9.36 ± 0.43	9.72 ± 0.63	9.17 ± 0.64	8.98 ± 0.63	7.89 ± 0.44

5.6 Discussion

Normal Vibration Holography was tested on simulations, homogeneous and heterogeneous phantoms. For simulations, where the propagation was unperturbed by the medium, it was possible to properly rebuild the speed map despite the added noise. For both media (homogeneous and heterogeneous) the estimated values were near to the established speed value when simulating, yielding a maximum accuracy error of 4.5%.

The next stage was to perform experiments on gelatin-based phantoms. From the interference patterns formed, it is possible to make some comments. As can be seen in Figure 5.5, it is noticeable the effect of attenuation in the interference pattern. According to the frequency and the amplitude used for tissue excitation, the valid region for interference pattern analysis can vary. Thus, although all the speed maps are from the same phantom, the represented area is not the same. When forming the speed map, the image reflects the homogeneous nature of the tissue, with a mean value close to the ground truth of 2.64 m/s. Nevertheless, using a single frequency and estimating shear speed from

a single interference pattern may lead to artifacts appearance in the speed map. Then, the estimation can be improved by considering more patterns at a slight different frequency and combining the results obtained.

This approach was used for the heterogeneous phantom analysis, using five single frequencies and perform experiments in the same region of interest for all of them. The results presented in table 5.2 describe a estimation that moves away for the last frequency considered. Overall, the results are consistent with the mechanical measurements used as a reference. By averaging the speed maps obtained with frequencies 296, 298 and 300 Hz, a speed map with background shear speed of 5.21 ± 5.16 m/s and inclusion shear speed of 9.28 ± 0.46 m/s. Since the ground truth is 5.01 m/s for the background and 10.04 m/s for the inclusion, the error estimation is 3.99% and 7.57 % respectively.

From the elastograms for the heterogeneous case presented, it is noticeable the presence of several artifacts, mainly in the borders of the region of interest. A source of error could be the attenuation induced in the interference pattern, which attenuates the intensity and makes difficult the correct phase identification, as well as reduced the CNR in the image. A better denoising step seems to be ideal to overcome this problem, specifically the application of time-gain compensation techniques. Likewise, a more robust algorithm than phase derivative could yield images of better quality and with less artifacts in the region of interest.

Chapter 6

Summary

Two elastographic techniques based on mechanical external vibration were evaluated: Vibro-elastography and Normal Vibration Holography.

Vibro-elastography was at first instance tested on a calibrated breast phantom, which has a background of 20 ± 5KPa and inclusions of at least the double of stiffness than the background. Several elastograms were obtained while changing the frequency excitation from 170 to 240 Hz. In the same way, a gelatin phantom was used, using an excitation frequency ranging from 100 to 300 Hz. Results suggest a good agreement between the estimated elasticity values with the reported values by the manufacturer and the reference values calculated, respectively. The trend of the estimation is to oscillate around the reported values. On the other hand, lateral resolution measurements yields good results, exhibiting an expected behavior according literature. Then, as frequency increases, the value decreases. In fact, by comparing the metrics obtained with the reported by Ormachea [37], results seem to indicate that Vibro-elastography has a similar lateral resolution than other steady-state techniques. Furthermore, contrast also oscillates inside the expected range of $[1 - 2.33]$ for the calibrated phantom and around 0.85 por the gelatin-based one. CNR values are in agreement with the reported previously by Mahdavi [39], presenting an stable trend for the frequencies used.

The ex-vivo experiments were used as a prelude for a posterior in-vivo application. For this purpose, an excised pig kidney with a homogeneous superficial region was employed for analysis. Elastograms were acquired from three different samples after careful conservation and within the first 12 hours of being excised. The mean estimation obtained also matches with the values reported by Caitlin et. al [36] for ex-vivo pig kidney at 0 mmHg of internal pressure. Since the frequencies selected worked well in ex-vivo tissue, we found appropriate to continue working with the same set for clinical cases.

In-vivo experiments were carried out at Oncosalud Health Center, in collaboration with physicians and radiologist. Signed consent was explained to patients who were going to pass biopsy exam, and the ones who agreed to collaborate in the study, were examined using the Vibro-elastography system. Eighteen patients were analyzed, and their elastography results were correlated with pathological ones. Then, by selecting two features: lesion stiffness and ratio between lesion and background stiffness, a liner classification was performed. In that way it was possible to differentiate between patients who were diagnose with benign or malignant cancer. Nevertheless, the distinction was not totally clear, since both benign and malignant cases presented just a small difference in elasticity values, which results in a concentration in the central region of the classification graphic. This can be attributed to the fact that histological grades in malignant cases were intermediate at maximum. Elasticity values found

for healthy breast (parenchyma layer) are similar to graphics presented by Barr [45] for another elastographic technique (Shear wave elastography). Undoubtedly, more patients will make possible to refine the results obtained. Examination of patients with a higher degree of the disease would bring interesting results to this study.

A novel setup based on Shear Wave Holography was presented in this thesis. The theory as well as the detailed experimental setup was shown. When applying on a tissue, a static interference pattern was formed, processed by using the phase derivative algorithm in the propagation direction. Simulations as well as experiments on homogeneous and heterogeneous phantoms were carried out, yielding accurate results when compared to mechanical stress-relaxation tests. On one hand, the elastograms were uniform for homogeneous cases; in the other hand, the elastograms for heterogeneous cases presented several artifacts, mainly in the borders of the region of interest. A source of error could be the attenuation induced in the interference pattern, which attenuates the intensity and makes difficult the correct phase identification, as well as reduced the CNR in the image. A better denoising step seems to be ideal to overcome this problem, specifically the application of time-gain compensation techniques. Likewise, a more robust algorithm than phase derivative could yield images of better quality and with less artifacts in the region of interest. However, it is worth to mention that it is the first experiment using Shear Wave Holography with normal vibration. This is one step closer to having practical clinical applications of this elastographic technique.

Appendices

Appendix A

In-vivo images acquired with Vibro-elastography

This appendix shows the B-mode and elastographic images for each of the 18 patients participating in the study. In addition, the biopsy result is described.

Patient 1

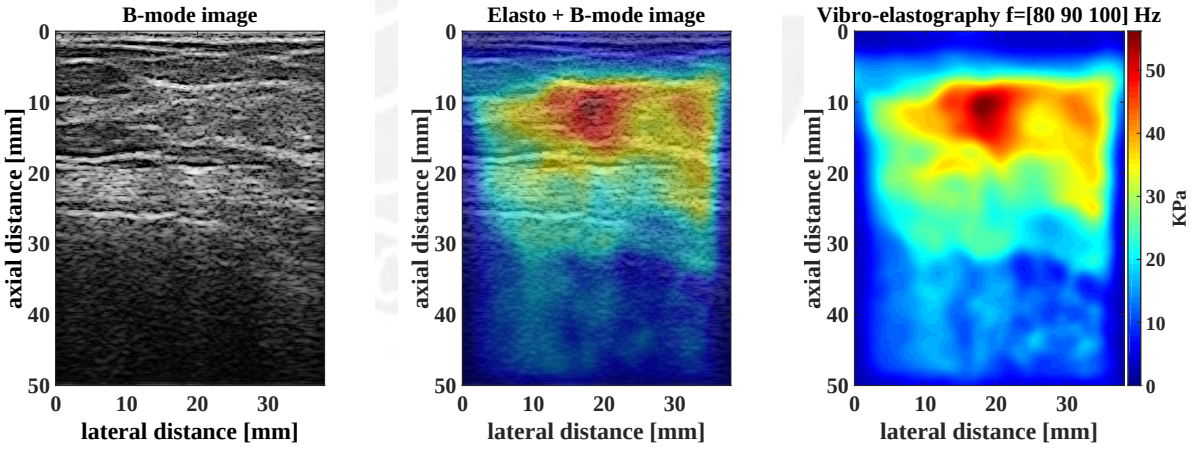

(a) (b) (c)

Figure 1.1: (a) B-mode, (b) Overlap elastography and B-mode and (c) Elastography images corresponding to the patient 1.
Background stiffness: 29.21 ± 4.77 KPa Inclusion stiffness: 51.76 ± 2.19 KPa
Biopsy result: Fibroadenomatoid changes. Free of malignant neoplasia.

Patient 2

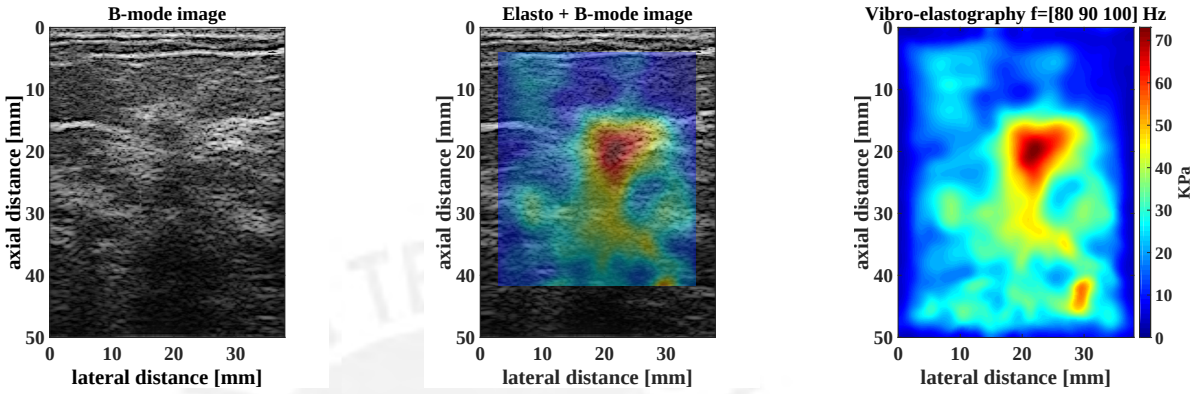

(a) (b) (c)

Figure 1.2: (a) B-mode, (b) Overlap elastography and B-mode and (c) Elastography images corresponding to the patient 2.
Background stiffness: 30.35 ± 7.70 KPa Inclusion stiffness: 67.84 ± 2.96 KPa
Biopsy result: Infiltrating breast carcinoma, ductal variety. Intermediate histological grade (2-2-2)

Patient 3

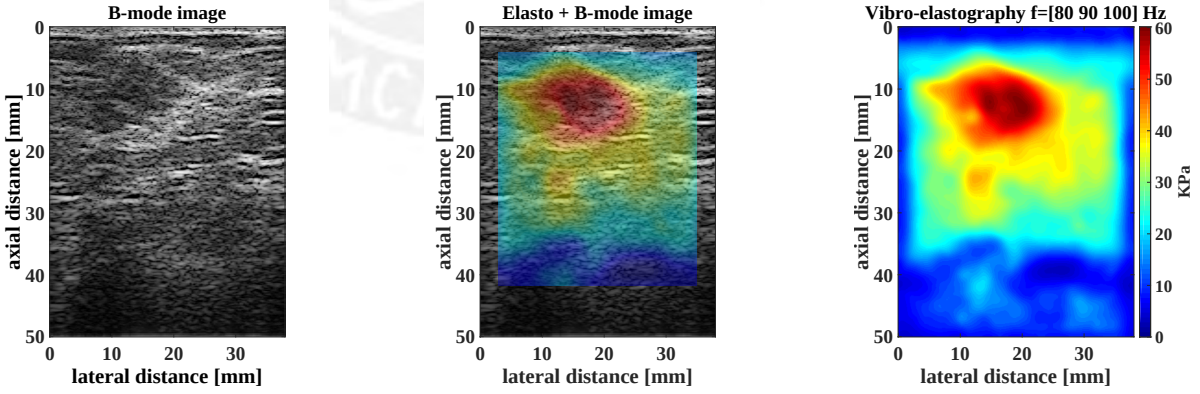

(a) (b) (c)

Figure 1.3: (a) B-mode, (b) Overlap elastography and B-mode and (c) Elastography images corresponding to the patient 3.
Background stiffness: 30.88 ± 5.33 KPa Inclusion stiffness: 54.77 ± 3.28 KPa
Biopsy result: Five samples were taken. 4 of lymph nodes (negative) and the last in breast, giving infiltrating carcinoma of the breast. Histological grade combined: Intermediate (3-2-1).

Patient 4

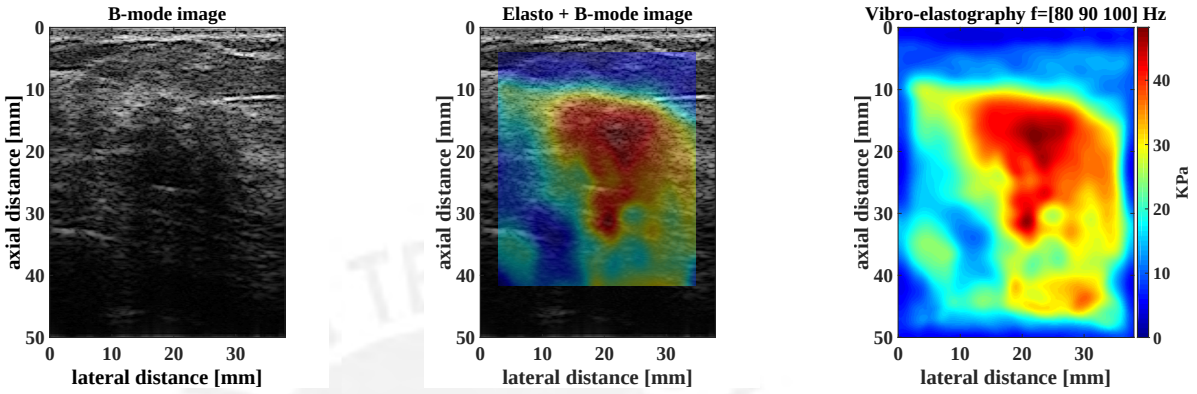

(a) (b) (c)

Figure 1.4: (a) B-mode, (b) Overlap elastography and B-mode and (c) Elastography images corresponding to the patient 4.
Background stiffness: 21.92 ± 6.61 KPa Inclusion stiffness: 44.21 ± 1.85 KPa
Biopsy result: Compatible with fibroadenoma. Free of malignant neoplasia.

Patient 5

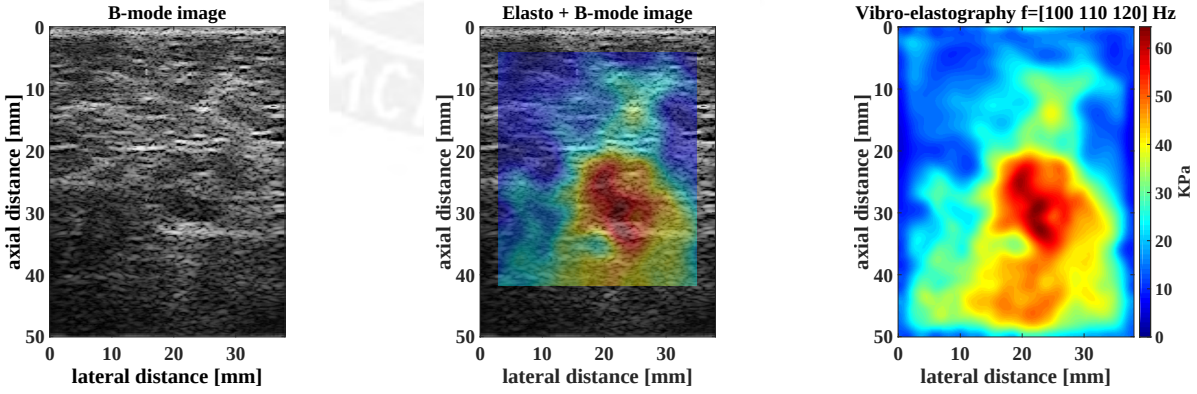

(a) (b) (c)

Figure 1.5: (a) B-mode, (b) Overlap elastography and B-mode and (c) Elastography images corresponding to the patient 5.
Background stiffness: 29.81 ± 6.36 KPa Inclusion stiffness: 55.81 ± 4.20 KPa
Biopsy result: Mature lymphoid tissue. There is no malignant neoplasia.

Patient 6

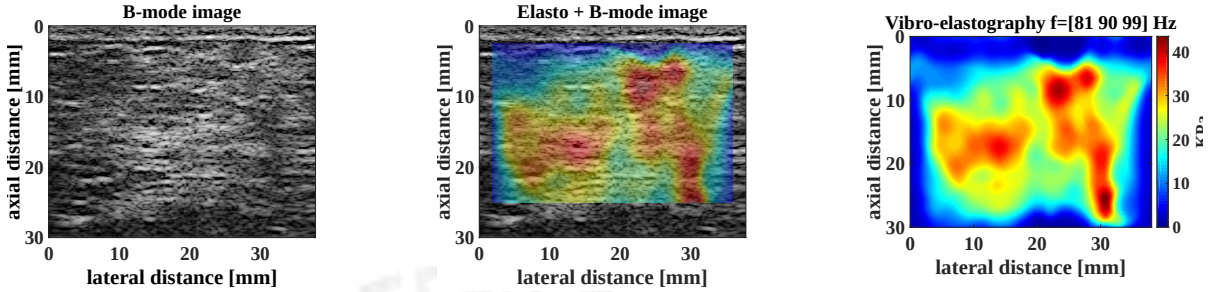

(a) (b) (c)

Figure 1.6: (a) B-mode, (b) Overlap elastography and B-mode and (c) Elastography images corresponding to the patient 6.
Background stiffness: 23.15 ± 5.59 KPa Inclusion stiffness: 39.72 ± 1.19 KPa
Biopsy result: Intraductal papillomas. Free from malignant neoplasia.

Patient 7

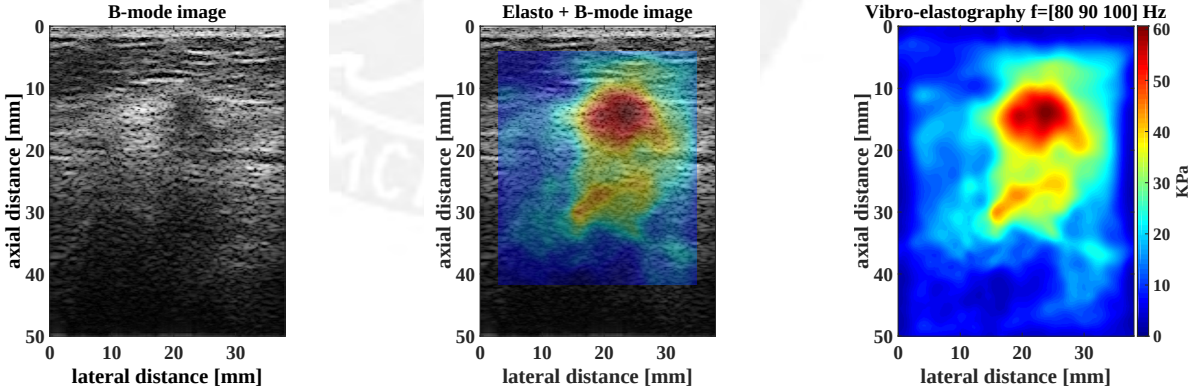

(a) (b) (c)

Figure 1.7: (a) B-mode, (b) Overlap elastography and B-mode and (c) Elastography images corresponding to the patient 7.
Background stiffness: 23.34 ± 8.21 KPa Inclusion stiffness: 56.32 ± 2.16 KPa
Biopsy result: Infiltrating breast carcinoma.

Patient 8

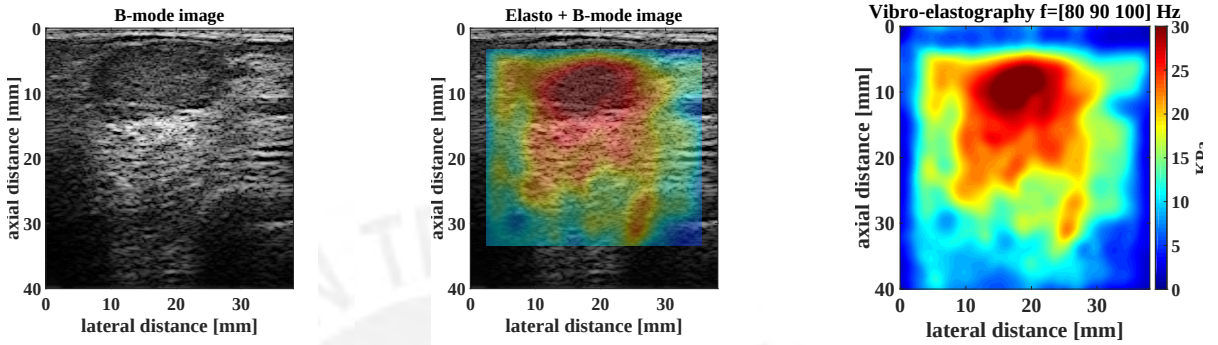

(a) (b) (c)

Figure 1.8: (a) B-mode, (b) Overlap elastography and B-mode and (c) Elastography images corresponding to the patient 8.
Background stiffness: 16.14 ± 2.55 KPa Inclusion stiffness: 29.73 ± 1.99 KPa
Biopsy result: Fibroepithelial lesion with cell stroma. Surgical excision of the lesion was suggested.

Patient 9

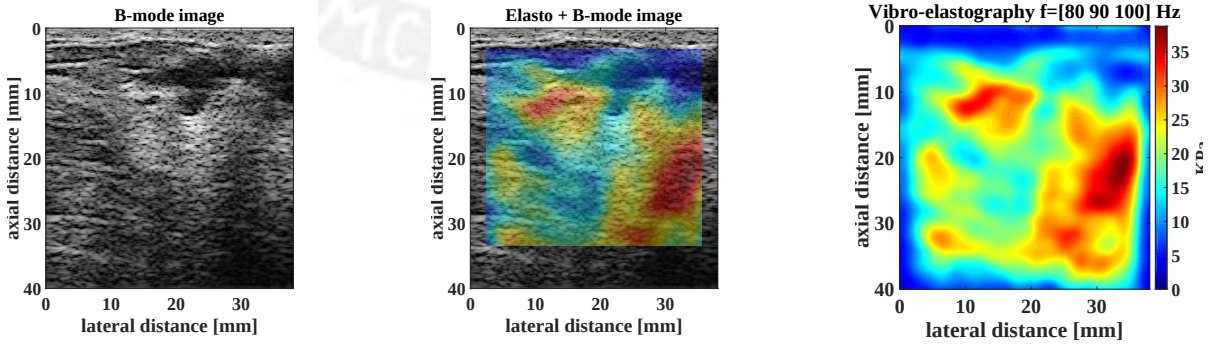

(a) (b) (c)

Figure 1.9: (a) B-mode, (b) Overlap elastography and B-mode and (c) Elastography images corresponding to the patient 9.
Background stiffness: 19.16 ± 3.84 KPa Inclusion stiffness: 9.00 ± 2.11 KPa
Biopsy result: Adenosis, ductal dilatation. There is no malignant neoplasia.

Patient 10

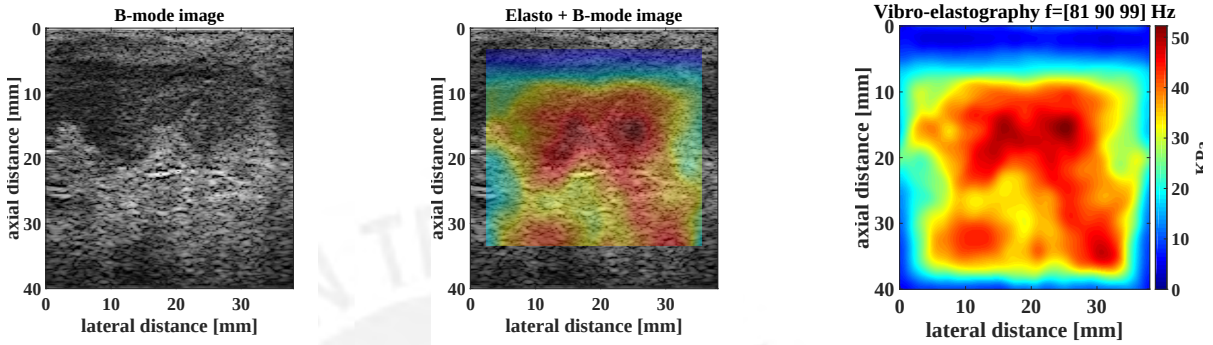

(a) (b) (c)

Figure 1.10: (a) B-mode, (b) Overlap elastography and B-mode and (c) Elastography images corresponding to the patient 10.
Background stiffness: 29.65 ± 7.39 KPa Inclusion stiffness: 46.82 ± 1.97 KPa
Biopsy result: Infiltrating carcinoma. Histological grade: intermediate (3-2-1).

Patient 11

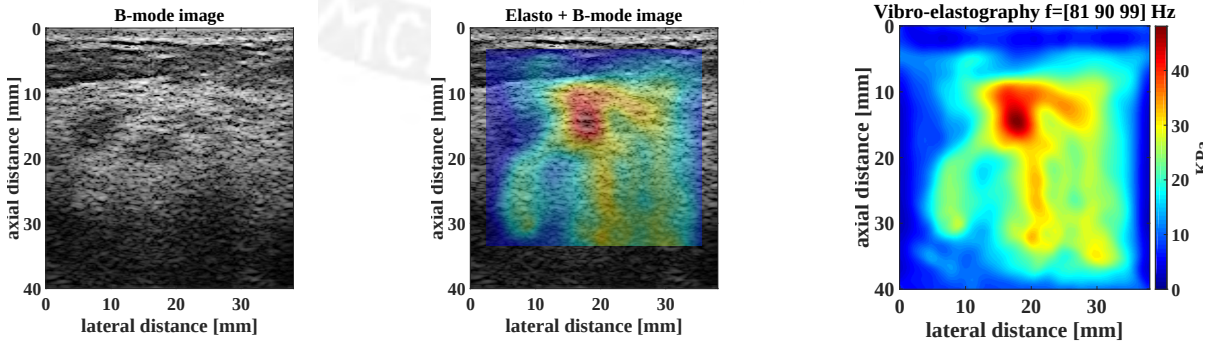

(a) (b) (c)

Figure 1.11: (a) B-mode, (b) Overlap elastography and B-mode and (c) Elastography images corresponding to the patient 11.
Background stiffness: 22.24 ± 5.80 KPa Inclusion stiffness: 44.56 ± 1.80 KPa
Biopsy result: Nodular adenosis. There is no malignant neoplasia.

Patient 12

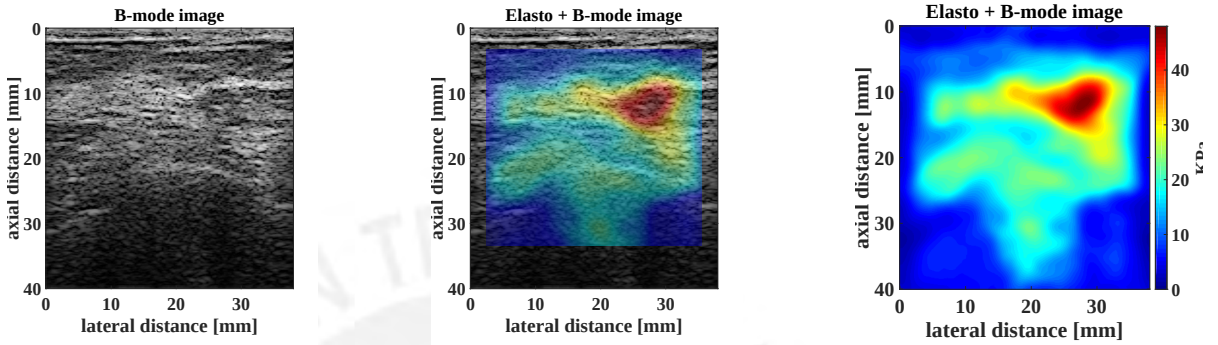

(a) (b) (c)

Figure 1.12: (a) B-mode, (b) Overlap elastography and B-mode and (c) Elastography images corresponding to the patient 12.
Background stiffness: 20.99 ± 3.74 KPa Inclusion stiffness: 44.62 ± 1.97 KPa
Biopsy result: Papillary injury with apocrine changes.

Patient 13

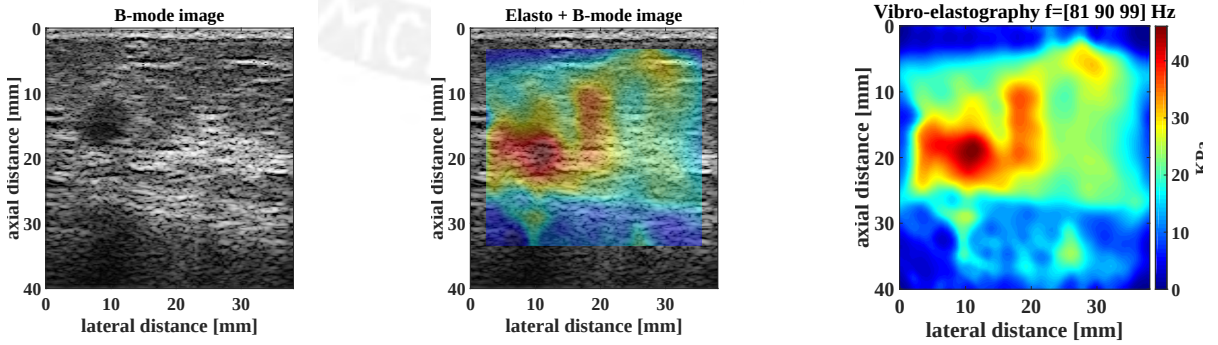

(a) (b) (c)

Figure 1.13: (a) B-mode, (b) Overlap elastography and B-mode and (c) Elastography images corresponding to the patient 13.
Background stiffness: 20.77 ± 5.49 KPa Inclusion stiffness: 42.75 ± 1.85 KPa
Biopsy result: Papillary compatible papilloma lesion.

Patient 14

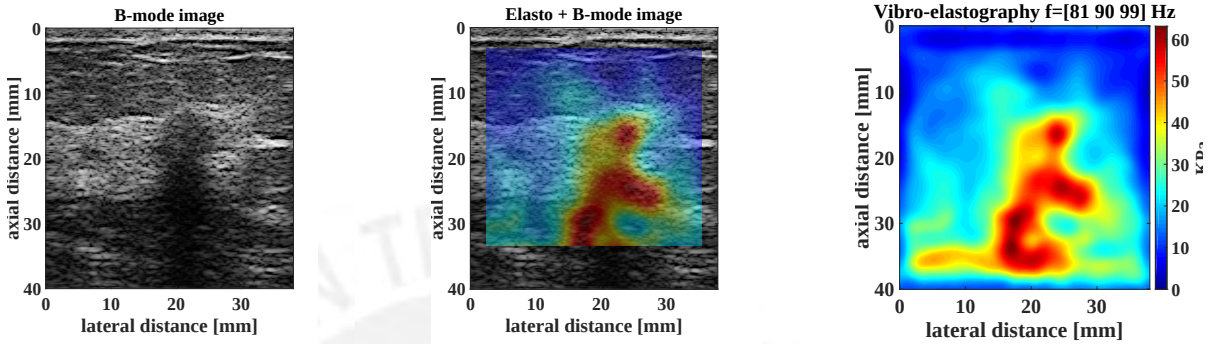

(a) (b) (c)

Figure 1.14: (a) B-mode, (b) Overlap elastography and B-mode and (c) Elastography images corresponding to the patient 14.
Background stiffness: 27.35 ± 6.19 KPa Inclusion stiffness: 55.39 ± 2.27 KPa
Biopsy result: Infiltrating carcinoma. Histological grade: intermediate (2-2-2).

Patient 15

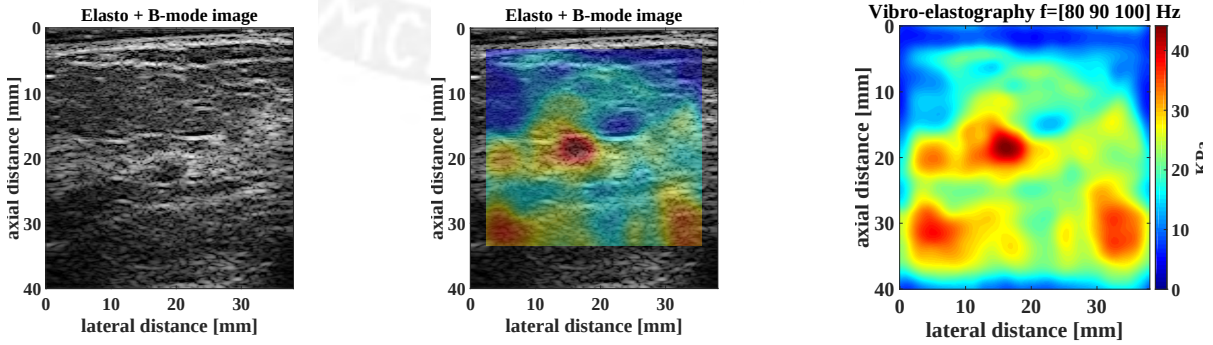

(a) (b) (c)

Figure 1.15: (a) B-mode, (b) Overlap elastography and B-mode and (c) Elastography images corresponding to the patient 15.
Background stiffness: 22.16 ± 4.16 KPa Inclusion stiffness: 41.80 ± 1.39 KPa
Biopsy result: Hialinized fibroepitelial injury. Malignant neoplasia is not observed.

Patient 16

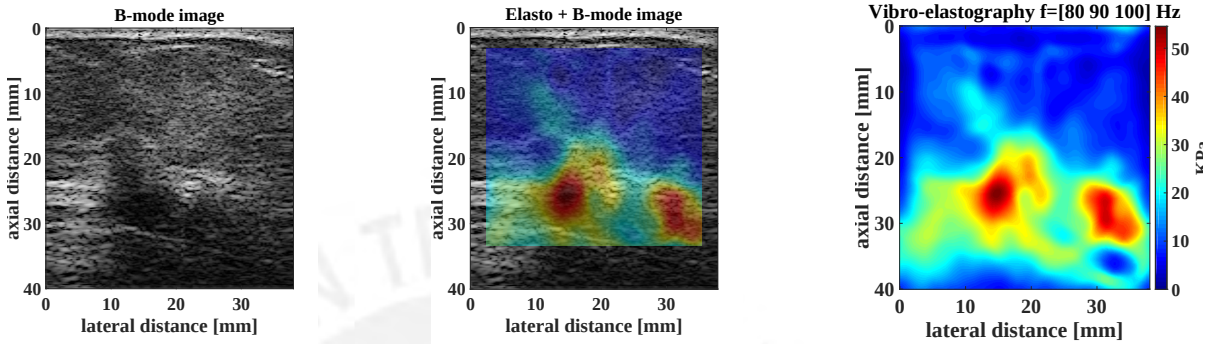

(a) (b) (c)

Figure 1.16: (a) B-mode, (b) Overlap elastography and B-mode and (c) Elastography images corresponding to the patient 16.
Background stiffness: 24.23 ± 5.94 KPa Inclusion stiffness: 51.30 ± 1.72 KPa
Biopsy result: Infiltrant carcinoma of breast, ductal variety. Histological degree: intermediate (2-2-2).

Patient 17

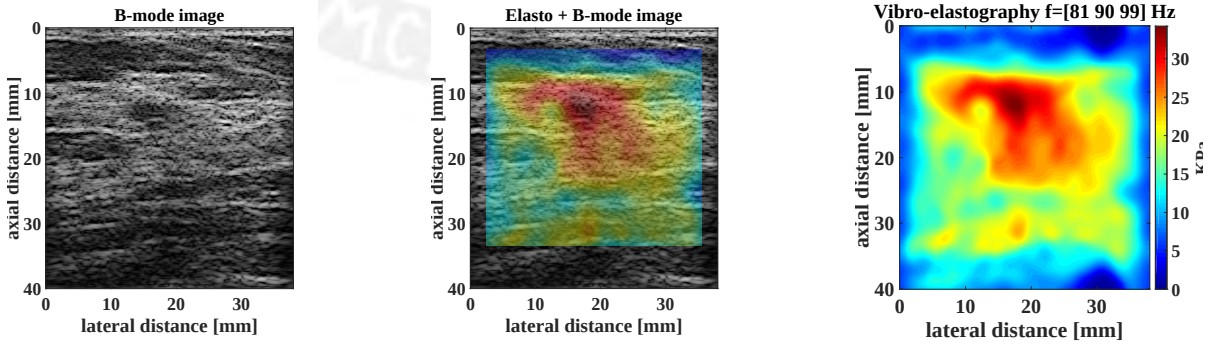

(a) (b) (c)

Figure 1.17: (a) B-mode, (b) Overlap elastography and B-mode and (c) Elastography images corresponding to the patient 17.
Background stiffness: 17.60 ± 3.00 KPa Inclusion stiffness: 32.53 ± 0.90 KPa
Biopsy result: Usual denosis. Usual hyperplasia and florida focal. Free from malignant neoplasia.

Patient 18

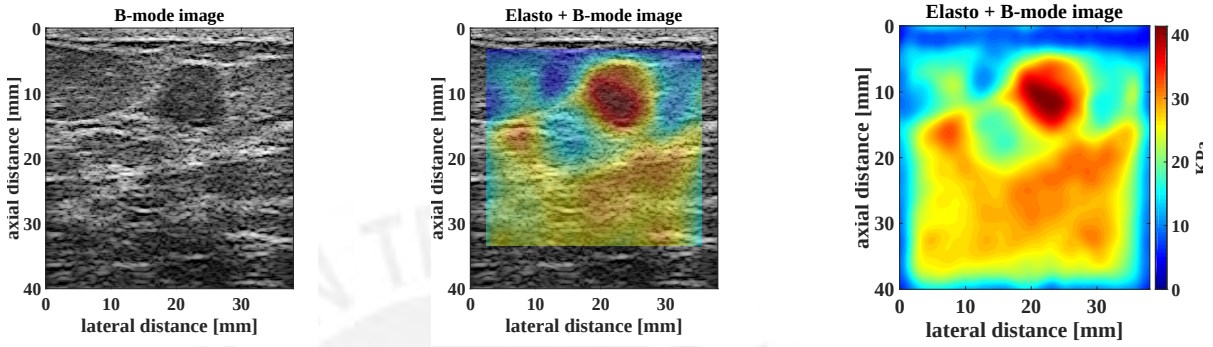

(a) (b) (c)

Figure 1.18: (a) B-mode, (b) Overlap elastography and B-mode and (c) Elastography images corresponding to the patient 18.
Background stiffness: 21.50 ± 4.03 KPa Inclusion stiffness: 37.42 ± 2.86 KPa
Biopsy result: Benign fibroepitelial neoplasia, compatible with fibroadenoma. Some focal characteristics are of phyllodes type. Free from malignant neoplasia.

Bibliography

[1] Cancer Statistics, "Cancer statistics, 2017," 2017.

[2] Ministerio de Salud del Perú, "Análisis de la situación del cáncer en el perú 2013," 2013.

[3] Kenneth Hoyt, Benjamin Castaneda, and Kevin J Parker, "Two-dimensional sonoelastographic shear velocity imaging," *Ultrasound in medicine & biology*, vol. 34, no. 2, pp. 276–288, 2008.

[4] Kenneth Hoyt, Timothy Kneezel, Benjamin Castaneda, and Kevin J Parker, "Quantitative sonoelastography for the in vivo assessment of skeletal muscle viscoelasticity," *Physics in medicine and biology*, vol. 53, no. 15, pp. 4063, 2008.

[5] Jonathan Ophir, Ignacio Cespedes, Hm Ponnekanti, Youseph Yazdi, and Xin Li, "Elastography: a quantitative method for imaging the elasticity of biological tissues," *Ultrasonic imaging*, vol. 13, no. 2, pp. 111–134, 1991.

[6] Robert M Lerner, SR Huang, and Kevin J Parker, ""sonoelasticity" images derived from ultrasound signals in mechanically vibrated tissues," *Ultrasound in medicine & biology*, vol. 16, no. 3, pp. 231–239, 1990.

[7] R Muthupillai, DJ Lomas, PJ Rossman, James F Greenleaf, et al., "Magnetic resonance elastography by direct visualization of propagating acoustic strain waves," *Science*, vol. 269, no. 5232, pp. 1854, 1995.

[8] Joseph M Schmitt, "Oct elastography: imaging microscopic deformation and strain of tissue," *Optics express*, vol. 3, no. 6, pp. 199–211, 1998.

[9] J-L Gennisson, Thomas Deffieux, Mathias Fink, and Michaël Tanter, "Ultrasound elastography: principles and techniques," *Diagnostic and interventional imaging*, vol. 94, no. 5, pp. 487–495, 2013.

[10] C Balleyguier, S Canale, W Ben Hassen, P Vielh, EH Bayou, MC Mathieu, C Uzan, C Bourgier, and C Dromain, "Breast elasticity: principles, technique, results: an update and overview of commercially available software," *European Journal of Radiology*, vol. 82, no. 3, pp. 427–434, 2013.

[11] Jeremy J Dahl, Gianmarco F Pinton, Mark L Palmeri, Vineet Agrawal, Kathryn R Nightingale, and Gregg E Trahey, "A parallel tracking method for acoustic radiation force impulse imaging," *IEEE transactions on ultrasonics, ferroelectrics, and frequency control*, vol. 54, no. 2, 2007.

[12] Marie Tabaru, Hideki Yoshikawa, Takashi Azuma, Rei Asami, and Kunio Hashiba, "Experimental study on temperature rise of acoustic radiation force elastography," *Journal of Medical Ultrasonics*, vol. 39, no. 3, pp. 137–146, 2012.

[13] Giovanna Ferraioli, Carmine Tinelli, Barbara Dal Bello, Mabel Zicchetti, Gaetano Filice, and Carlo Filice, "Accuracy of real-time shear wave elastography for assessing liver fibrosis in chronic hepatitis c: A pilot study," *Hepatology*, vol. 56, no. 6, pp. 2125–2133, 2012.

[14] Giovanna Ferraioli, Carmine Tinelli, Mabel Zicchetti, Elisabetta Above, Gianluigi Poma, Marta Di Gregorio, and Carlo Filice, "Reproducibility of real-time shear wave elastography in the evaluation of liver elasticity," *European journal of radiology*, vol. 81, no. 11, pp. 3102–3106, 2012.

[15] Mitsuhiro Tozaki and Eisuke Fukuma, "Pattern classification of shearwavetm elastography images for differential diagnosis between benign and malignant solid breast masses," *Acta Radiologica*, vol. 52, no. 10, pp. 1069–1075, 2011.

[16] Alexandra Athanasiou, Anne Tardivon, Mickael Tanter, Brigitte Sigal-Zafrani, Jeremy Bercoff, Thomas Deffieux, Jean-Luc Gennisson, Mathias Fink, and Sylvia Neuenschwander, "Breast lesions: quantitative elastography with supersonic shear imaging—preliminary results 1," *Radiology*, vol. 256, no. 1, pp. 297–303, 2010.

[17] Andrew Evans, Patsy Whelehan, Kim Thomson, Denis McLean, Katrin Brauer, Colin Purdie, Lee Jordan, Lee Baker, and Alastair Thompson, "Quantitative shear wave ultrasound elastography: initial experience in solid breast masses," *Breast Cancer Research*, vol. 12, no. 6, pp. R104, 2010.

[18] A Goddi, M Bonardi, and S Alessi, "Breast elastography: a literature review," *Journal of ultrasound*, vol. 15, no. 3, pp. 192–198, 2012.

[19] Tomy Varghese, "Quasi-static ultrasound elastography," *Ultrasound clinics*, vol. 4, no. 3, pp. 323–338, 2009.

[20] Brian S Garra, E Ignacio Cespedes, Jonathan Ophir, Stephen R Spratt, Rebecca A Zuurbier, Colette M Magnant, and Marie F Pennanen, "Elastography of breast lesions: initial clinical results.," *Radiology*, vol. 202, no. 1, pp. 79–86, 1997.

[21] Timothy J Hall, Yanning Zhu, and Candace S Spalding, "In vivo real-time freehand palpation imaging," *Ultrasound in medicine & biology*, vol. 29, no. 3, pp. 427–435, 2003.

[22] Mallika Sridhar and Michael F Insana, "Ultrasonic measurements of breast viscoelasticity," *Medical physics*, vol. 34, no. 12, pp. 4757–4767, 2007.

[23] Hiroyasu Morikawa, *Real-time tissue elastography and transient elastography for evaluation of hepatic fibrosis*, INTECH Open Access Publisher Rijeka, 2012.

[24] Christian Vorländer, Jan Wolff, Said Saalabian, Robert H Lienenlüke, and Robert A Wahl, "Real-time ultrasound elastography—a noninvasive diagnostic procedure for evaluating dominant thyroid nodules," *Langenbeck's archives of surgery*, vol. 395, no. 7, pp. 865–871, 2010.

[25] Urszula Zaleska-DorobiszA, Krzysztof KaczorowskiB, Aleksander PawluśB, Agata PuchalskaB, and Marcin InglotB, "Ultrasound elastography–review of techniques and its clinical applications," *brain*, vol. 6, pp. 10–14, 2013.

[26] Abdurrahman Sagir, Andreas Erhardt, Marcus Schmitt, and Dieter Häussinger, "Transient elastography is unreliable for detection of cirrhosis in patients with acute liver damage," *Hepatology*, vol. 47, no. 2, pp. 592–595, 2008.

[27] Umberto Arena, Francesco Vizzutti, Giampaolo Corti, Silvia Ambu, Cristina Stasi, Silvia Bresci, Stefania Moscarella, Vieri Boddi, Antonio Petrarca, Giacomo Laffi, et al., "Acute viral hepatitis increases liver stiffness values measured by transient elastography," *Hepatology*, vol. 47, no. 2, pp. 380–384, 2008.

[28] Armen P Sarvazyan, Oleg V Rudenko, Scott D Swanson, J Brian Fowlkes, and Stanislav Y Emelianov, "Shear wave elasticity imaging: a new ultrasonic technology of medical diagnostics," *Ultrasound in medicine & biology*, vol. 24, no. 9, pp. 1419–1435, 1998.

[29] Jérémy Bercoff, Mickael Tanter, and Mathias Fink, "Supersonic shear imaging: a new technique for soft tissue elasticity mapping," *IEEE transactions on ultrasonics, ferroelectrics, and frequency control*, vol. 51, no. 4, pp. 396–409, 2004.

[30] Zhe Wu, *Shear wave interferometry and holography, an application of sonoelastography*, Ph.D. thesis, University of Rochester, 2005.

[31] Emre Turgay, Septimiu Salcudean, and Robert Rohling, "Identifying the mechanical properties of tissue by ultrasound strain imaging," *Ultrasound in medicine & biology*, vol. 32, no. 2, pp. 221–235, 2006.

[32] Jeffrey Michael Abeysekera, *Three dimensional ultrasound elasticity imaging*, Ph.D. thesis, University of British Columbia, 2016.

[33] Kishore Kumar, Maneesha E Andrews, V Jayashankar, Ashok K Mishra, and S Suresh, "Measurement of viscoelastic properties of polyacrylamide-based tissue-mimicking phantoms for ultrasound elastography applications," *IEEE Transactions on Instrumentation and Measurement*, vol. 59, no. 5, pp. 1224–1232, 2010.

[34] Man Zhang, Benjamin Castaneda, Zhe Wu, Priya Nigwekar, Jean V Joseph, Deborah J Rubens, and Kevin J Parker, "Congruence of imaging estimators and mechanical measurements of viscoelastic properties of soft tissues," *Ultrasound in medicine & biology*, vol. 33, no. 10, pp. 1617–1631, 2007.

[35] Herbert Kolsky, *Stress waves in solids*, vol. 1098, Courier Corporation, 1963.

[36] Caitlin Schneider, Mohammad Honarvar, Julio Lobo, Robert Rohling, Tim Salcudean, Samir Bidnur, and Christopher Nguan, "Blood pressure dependent elasticity measurements of porcine kidney ex-vivo," in *Ultrasonics Symposium (IUS), 2016 IEEE International*. IEEE, 2016, pp. 1–4.

[37] Juvenal Ormachea Quispe, "Evaluation of shear wave speed measurements using crawling waves sonoelastography and single tracking location acoustic radiation force impulse imaging," 2015.

[38] Stephen Rosenzweig, Mark Palmeri, Ned Rouze, Samantha Lipman, Evan Kulbacki, John Madden, Thomas Polascik, and Kathryn Nightingale, "Comparison of concurrently acquired in vivo 3d arfi and swei images of the prostate," in *Ultrasonics Symposium (IUS), 2012 IEEE International*. IEEE, 2012, pp. 97–100.

[39] Moradi M. Wen X. Morris W. J. Mahdavi, S. S. and S. E. Salcudean, "Evaluation of visualization of the prostate gland in vibro-elastography images," *Medical image analysis*, vol. 15, no. 4, pp. 589–600, 2011.

[40] Hani Eskandari, Septimiu E Salcudean, Robert Rohling, Ali Baghani, Samuel Frew, Paula B Gordon, and Linda Warren, "Identifying malignant and benign breast lesions using vibroelastography," in *Ultrasonics Symposium (IUS), 2013 IEEE International*. IEEE, 2013, pp. 25–28.

[41] Deniz Cebi Olgun, Bora Korkmazer, Fahrettin Kilic, Atilla Suleyman Dikici, Mehmet Velidedeoglu, Fatih Aydogan, Fatih Kantarci, and Mehmet Halit Yilmaz, "Use of shear wave elastography to differentiate benign and malignant breast lesions," *Diagnostic and Interventional Radiology*, vol. 20, no. 3, pp. 239, 2014.

[42] A Evans, P Whelehan, K Thomson, K Brauer, L Jordan, C Purdie, D McLean, L Baker, S Vinnicombe, and A Thompson, "Differentiating benign from malignant solid breast masses: value of shear wave elastography according to lesion stiffness combined with greyscale ultrasound according to bi-rads classification," *British journal of cancer*, vol. 107, no. 2, pp. 224–229, 2012.

[43] Mahdi Bayat, Max Denis, Adriana Gregory, Mohammad Mehrmohammadi, Viksit Kumar, Duane Meixner, Robert T Fazzio, Mostafa Fatemi, and Azra Alizad, "Diagnostic features of quantitative comb-push shear elastography for breast lesion differentiation," *PloS one*, vol. 12, no. 3, pp. e0172801, 2017.

[44] Bradley E Treeby and Benjamin T Cox, "k-wave: Matlab toolbox for the simulation and reconstruction of photoacoustic wave fields," *Journal of biomedical optics*, vol. 15, no. 2, pp. 021314–021314, 2010.

[45] Richard G Barr, "Sonographic breast elastography," *Journal of Ultrasound in Medicine*, vol. 31, no. 5, pp. 773–783, 2012.